PEER NGA-Subduction Project:

USGS Final Report

G12AP20008

Yousef Borzorgnia
Pacific Earthquake Engineering Research Center
University of California, Berkeley

Tadahiro Kishida
Pacific Earthquake Engineering Research Center
University of California, Berkeley

Jonathan P. Stewart
Department of Civil and Environmental Engineering
University of California, Los Angels

Robert E. Kayen
U.S. Geological Survey
Menlo Park, California

Pacific Earthquake Engineering Research Center

June 2013

ABSTRACT

NGA-Subduction (NGA-Sub) has been recently initiated by the Pacific Earthquake Engineering Research Center (PEER) with a plan for three phases. The scope of the Phase I of the NGA-Sub, the subject of this report, consists of three tasks: (a) Start to develop a comprehensive database of the ground motions recorded in subduction earthquakes and specifically include the data recorded in the M_w9.0 2011 Tohoku-oki Japan earthquake and the M_w8.8 2010 Maule Chile Earthquake; (b) Compare the recorded motions with the existing ground motion prediction equations (GMPEs) used in subduction zone regions; and (c) send a team of geotechnical engineers to Chile for the surface-wave measurements at the ground motion recording sites to characterize site response. Tasks (a) and (b) are funded by the USGS/NEHRP and FM Global funding, and Task (c), headed by Dr. Robert Kayen of the USGS, is funded by PEER's internal funding other than USGS/NEHRP and FM Global. This report is a collection of publications and reports related to these three tasks.

For Tasks (a) and (b): We started by collecting the recorded data in the 2011 Tohoku, Japan, and the 2010 Maule, Chile, earthquakes. The development of the database for these earthquakes has been completed and two paper publications summarize the efforts. The first paper is: "*Implications of Mw 9.0 Tohoku-oki Japan earthquake for ground motion scaling with source, path, and site parameters*", by Stewart, J. P., Midorikawa, S., Graves, R. W., Khodaverdi, K., Kishida, T., Miura, H., Bozorgnia, Y., and Campbell, K.W, to be published by Earthquake Spectra (2013). This paper is presented as the Chapter 1 of this report. The second paper is: "*Comparison of Ground Motion Attributes from 2011 Tohoku-oki Mainshock and Two Subsequent Events*" by Kishida, T., Stewart, J. P., Graves, R. W., Midorikawa, S., Miura, H., Bozorgnia, Y. and Campbell, K. W., published in the Proceedings 10th International Conference on Urban Earthquake Engineering, CUEE (2013). This paper is presented in Chapter 2 of this report.

Chapter 3 of this report is related to the Task (c), the field survey at strong motion stations in Chile. This Chapter consists of a report on "*Site Amplification Factors for 31 Chilean Seismometer Stations by Spectral Analysis of Surface Wave Dispersion Shaken During the Maule M8.8 Earthquake of 27 February 2010*" by Kayen, R. E., Carkin, B. D., Pinilla, C., Corbet, S., Ng, A., Gorbis, E. and Truong, C.

ACKNOWLEDGMENTS

This work was supported by the USGS Award number G12AP20008 and FM Global. The supports are gratefully acknowledged.

Any opinions, findings, and conclusions or recommendations expressed in this material are those of the authors and do not necessarily reflect those of the funding agencies.

CONTENTS

1 Implications of Recent Subduction Earthquakes for Ground Motion Scaling with Source, Path, and Site Parameters

The Mw9.0 Tohoku-oki Japan earthquake was extremely well recorded. We obtained the un-processed recordings from various organizations in Japan (KNET, KIKNET, and JMA), and processed 1,238 three-component accelerograms by applying component-specific low- and high-cut filters. Usable response spectral periods are from 0.01 sec to longer than 10 sec. The recordings have rupture distances between 44 km and 1,000 km. Time-averaged shear-wave velocities at the top 30-m of soil, V_{S30}, are calculated by the shear-wave velocity profile and correlations with geomorphology units. The results show that V_{S30} ranges from 90 to 1,900 m/s. The developed database is compared with the predictions of the exiting ground motion prediction equations (GMPEs) for subduction zones. The data from the 2010 Chile earthquake were also used to evaluate the magnitude scaling of ground motions. For the Tohoku earthquake, event terms are calculated at the fault distance of 100 km, which are generally positive (indicating model underprediction) at short periods and zero or negative (overprediction) at long periods. Site amplification with V_{S30} is evaluated from high to low frequencies. The results of these analyses are presented in a paper entitled: "*Implications of Mw 9.0 Tohoku-oki Japan earthquake for ground motion scaling with source, path, and site parameters*", by Stewart, J. P., Midorikawa, S., Graves, R. W., Khodaverdi, K., Kishida, T., Miura, H., Bozorgnia, Y., and Campbell, K. W., to be published by Earthquake Spectra (2013). The paper is presented in the following section.

Implications of the M_w9.0 Tohoku-Oki Earthquake for Ground Motion Scaling with Source, Path, and Site Parameters

Jonathan P. Stewart,[a] M.EERI, Saburoh Midorikawa,[b] M.EERI, Robert W. Graves,[c] M.EERI, Khatareh Khodaverdi,[a] S.M.EERI, Tadahiro Kishida,[d] M.EERI, Hiroyuki Miura,[b] M.EERI, Yousef Bozorgnia,[d] M.EERI, and Kenneth W. Campbell[e] M.EERI

The M_w9.0 Tohoku-oki Japan earthquake produced approximately 2,000 ground motion recordings. We consider 1,238 three-component accelerograms corrected with component-specific low-cut filters. The recordings have rupture distances between 44 km and 1,000 km, time-averaged shear wave velocities of $V_{S30} = 90$ m/s to 1,900 m/s, and usable response spectral periods of 0.01 sec to >10 sec. The data support the notion that the increase of ground motions with magnitude saturates at large magnitudes. High-frequency ground motions demonstrate faster attenuation with distance in backarc than in forearc regions, which is only captured by one of the four considered ground motion prediction equations for subduction earthquakes. Recordings within 100 km of the fault are used to estimate event terms, which are generally positive (indicating model underprediction) at short periods and zero or negative (overprediction) at long periods. We find site amplification to scale minimally with V_{S30} at high frequencies, in contrast with other active tectonic regions, but to scale strongly with V_{S30} at low frequencies. [DOI: 10.1193/1.4000115]

INTRODUCTION

The M_w9.0 Tohoku-oki earthquake occurred on 11 March 2011 off the Pacific Coast of Japan. This earthquake is associated with the subduction process of the Pacific plate beneath the North American (continental) plate at the Japan Trench, which occurs with a convergence rate of about 8–9 cm/yr. The earthquake resulted from thrust-faulting at the interface between the two plates, which has produced many large historic earthquakes, including the 1896 Meiji-Sanriku earthquake (estimated M_w8.5) and nine events of magnitude 7 or greater in the modern instrumental era (since 1973, when the Japan Meteorological Agency has distributed relatively high quality seismic data), including the 1978 Miyagi earthquake (M_w7.4). The USGS (2012) placed the main shock hypocenter about 129 km east of Sendai (38.297°N, 142.372°E) at a depth of 30 km (USGS 2012). The rupture length (along strike) extended for

[a] University of California, Los Angeles, CA, jstewart@seas.ucla.edu
[b] Tokyo Institute of Technology, Yokohama, Japan
[c] US Geological Survey, Pasadena, CA
[d] PEER Center, University of California, Berkeley, CA
[e] EQECAT, Inc., Beaverton, OR

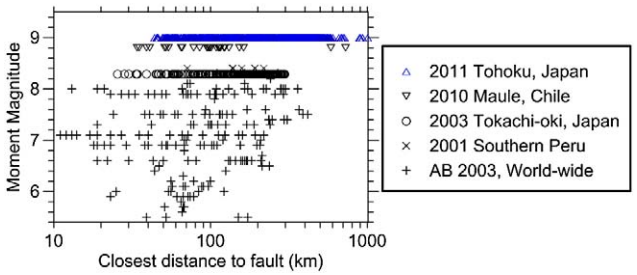

Figure 1. Distribution of strong motion data for interface subduction zone earthquakes. Data taken from electronic supplement to Atkinson and Boore (2003) for data prior to 2001, Rodriguez-Marek et al. (2010) for the 2001 Southern Peru earthquake, Zhao (2011) for the 2003 Tokachi-oki earthquake, and Boroschek et al. (2012) for the Maule earthquake.

approximately 480 km, from the north end of Honshu Island to Tokyo Bay in the south, and had a down-dip width of approximately 180 km. The event produced a destructive tsunami, devastating coastal areas including catastrophic damage at the Fukushima nuclear power plant (e.g., Mori et al. 2013), extensive ground failure from liquefaction and slope instability (e.g., Cox et al. 2013), but only modest shaking-related damage (e.g., Okazaki et al. 2013, Kawashima and Buckle 2013).

The Tohoku earthquake is the largest magnitude event to have produced strong motion recordings. Figure 1 shows the strong motion data distribution for worldwide subduction zone interface earthquakes through 2011. The data shown in Figure 1 are from the data set used by Atkinson and Boore (2003), supplemented with the more recent events listed in the legend and caption. The general characteristics of the ground motions from this major event have been described previously by Furumura et al. (2011), Skarlatoudis and Papazachos (2012), and Midorikawa et al. (2012). In the present work, we extend the previous studies by performing more quantitative residuals analysis to investigate event terms, distance attenuation trends, and site effects.

In this article, we begin by describing the geologic and tectonic setting, the seismic sequence, and alternate finite-fault representations of the source from the literature. We select a finite-fault model for use in site-to-source distance calculations. We describe the ground motion database including the record processing procedures that were applied and the evaluation of site conditions from available data resources. We then compare observed spectral accelerations to predictions from four ground motion prediction equations (GMPEs), three of which are international models for subduction zone earthquakes, and one of which is Japan-specific. We formally examine issues related to magnitude-scaling, distance-scaling, site effects, and within-event data dispersion. These results will be directly applicable to the development of next-generation GMPEs for interface subduction zone earthquakes. Analyses of this type have not been performed previously on the Tohoku data set, although where related prior work has been performed (e.g., on the distance attenuation issue), we compare our results to those described previously.

SETTING AND SOURCE DESCRIPTION

REGIONAL GEOLOGY

Figure 2 depicts surface geological conditions in the Tohoku region, as well as the Kanto region to the south, which includes Tokyo. Starting from the north end of the earthquake region in the Iwate Prefecture, Figure 2 shows the Kitakami Mountains along the Ria coast, which are composed of Paleozoic-Mesozoic sedimentary rocks, accretionary complexes, and Cretaceous felsic plutonic rocks (Geospatial Information Authority of Japan 1997). As is typical of island arc systems, behind (west of) the coastal range is a sedimentary depression, which is bounded to the west by the igneous (volcanic) Ou Mountain Range that forms the central backbone of northern Honshu. The Ou range is composed of volcanic and sedimentary rocks from the Late Oligocene and deposits from Quaternary volcanoes, and extends as far south as the Kanto Plain. In northern Honshu, the Ou range is the volcanic front that forms the boundary between the forearc and backarc regions, as discussed below.

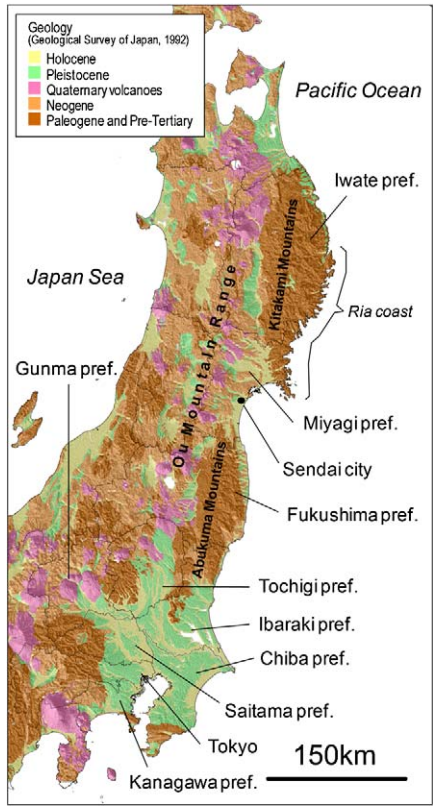

Figure 2. Generalized geological map with shaded relief of topography in Tohoku and Kanto regions of Japan. Source: Geological Survey of Japan (1992).

The Sendai Plain occurs at the southwest end of the Kitakami Mountains in the Miyagi Prefecture. The Sendai Plain is comprised of Holocene sediments and is bounded to the west by the Ou Mountain Range and to the south by the coastal Abukuma Mountains. The Abukuma Mountains are similar in composition to the Kitakami Mountains to the north, and as with the northern range, are bounded to the west by a sedimentary depression before reaching the Ou range.

At the south end of the earthquake region is the Kanto Plain, which includes the prefectures of Gunma, Tochigi, Ibaraki, Saitama, Chiba, Kanagawa, and Tokyo. The Kanto Plain is underlain by a large-scale Quaternary sedimentary basin having Holocene sediments in coastal areas and along major rivers to a maximum depth of about 50 m to 100 m. The depth of the sedimentary basin to the Pre-tertiary bedrock reaches approximately 3–4 km.

SEISMIC SEQUENCE

Figure 3 shows the epicenters of the 2011 Tohoku earthquake and its major ($M_w > 5$) aftershocks in the initial 24 hours. Additional information on fault dimensions, slip, and zones of high-frequency energy release are also shown, which are described in subsequent sections. Moment tensor solutions for the main shock and two large aftershocks (from JMA 2012) are also shown. The main shock moment tensor solution has a JMA seismic moment of 4.22×10^{22} N · m (4.5×10^{22} N · m from the USGS), a hypocentral depth from JMA of 24 km (30 km from the USGS), and a moment magnitude of $M_w = 9.0$ (from both JMA and the USGS). The moment tensor solutions indicate reverse faulting consistent with a megathrust earthquake. Most of the aftershocks are distributed within the boundaries of the finite-fault model shown in Figure 3, which is roughly 480 km along-strike by 180 km wide down-dip.

Figure 3 also shows a portion of the volcanic front near the study region in Japan. The volcanic front was defined by connecting the locations of major volcanic mountains, and is useful for delineating forearc and backarc regions. Variations in ground motion attenuation in the two regions are discussed subsequently in this article.

FINITE FAULT MODEL

Models of the rupture process for the Tohoku-oki main shock have been generated from a variety of data sources including geodetic, teleseismic, strong motion, and tsunami. Models generated from joint inversions of multiple data sets are presented by Ammon et al. (2011), Koketsu et al. (2011), Lee et al. (2011), Shao and Ji (2011), Simons et al. (2011), Yokota et al. (2011), and Wei et al. (2012). Simons et al. (2011) was among the first studies to identify the dual nature of the rupture process. In general, the shallow portion of the rupture (up-dip of the hypocenter) was characterized by large (>50 m) and relatively slow fault displacement, which created the devastating tsunami and generated most of the long-period ($T > 20$ s) seismic radiation. Deeper portions of the rupture had relatively low slip, but the slip occurred more quickly than on the shallow fault and resulted in the generation of significant shorter period ($T < 20$ s) seismic radiation. Additionally, since the deeper portion of the fault is much closer to Honshu, the strong ground shaking response on-shore was primarily controlled by the deeper rupture (Wei et al. 2012).

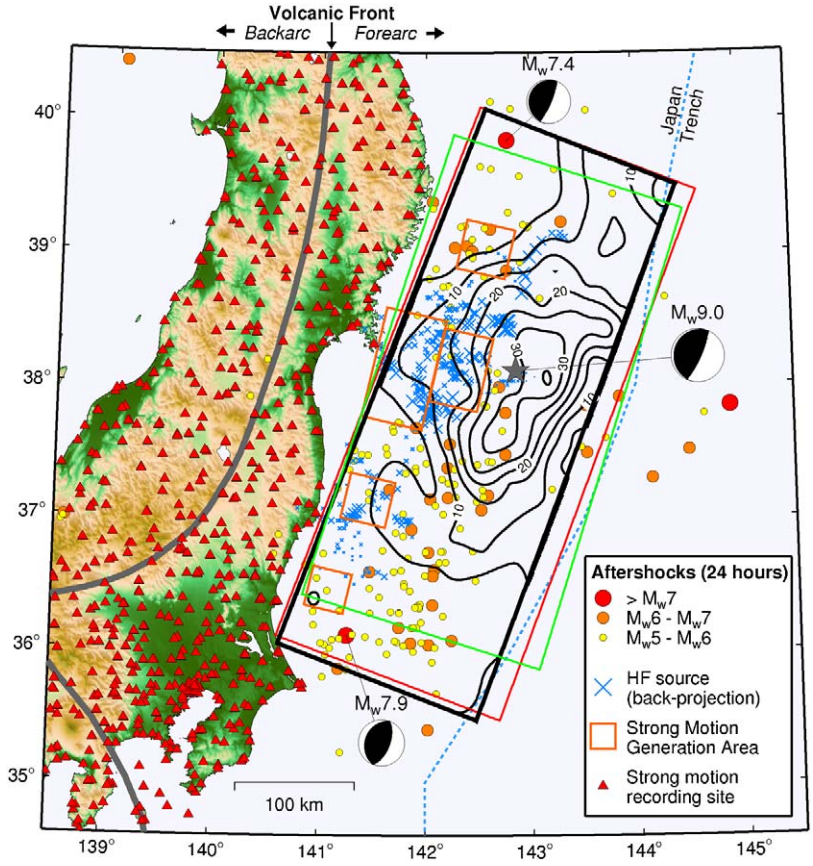

Figure 3. Map view showing surface projections of the three trimmed fault models (Yokota = black, Shao = green, Wei = red) along with the strong motion generation areas of Kurahashi and Irikura (2011; orange rectangles) and the high-frequency back-projection source locations of Meng et al. (2011; blue crosses). Contours indicate slip (m) for the Yokota rupture model. Colored circles show aftershocks within the first 24 hours following the main shock. Dashed blue line indicates location of Japan Trench and the gray star is the JMA epicenter of the main shock. The red triangles denote the locations of some of the strong motion recording sites considered in our analysis (additional stations were considered beyond the limits of the map).

Studies utilizing multiple data sets in their inversions highlight the importance of considering data spanning a broad frequency range. For example, Koketsu et al. (2011) demonstrate that inversions considering only strong motion data only recover slip on relatively deep portions of the fault, whereas inversions using only geodetic or tsunami data only recover slip on shallow portions of the fault. Combining multiple data sets in the inversion allows the recovery of both the large shallow slip and the relatively smaller displacement, but more seismically energetic, deep slip.

Accordingly, we restricted our analysis to models derived from multiple data sets, where one of the data sources includes strong ground motion data. In the present study, we have considered the models of Shao and Ji (2011), Yokota et al. (2011) and Wei et al. (2012). Slip distribution plots of the three models as projected in plan view are shown in the electronic supplement materials (Figure ES1), while Figure 3 shows slip contours for the Yokota et al. (2011) model. As with all slip model inversions, the resolution of smaller slip values has more uncertainty because larger slip patches dominate the solution. Since the maximum slip in these models is extremely large, ranging from 35 m to 63 m, we have chosen to truncate the slip at a minimum value of 3 m (in Figure ES1, open circles indicate subfaults with slip $\leq$ 3 m). The bounding rectangles shown in Figure ES1 and Figure 3 represent the fault surfaces of these models after trimming rows and columns in which slip on all subfaults is under 3 m, although no trimming was needed for the Yokota et al. (2011) model. The general patterns of slip in the three models are similar, being dominated by large slip on shallow portions of the fault.

Figure 3 shows that the two trimmed models and the Yokota et al. (2011) model are fairly similar, with the main differences being the somewhat shorter eastward (up-dip) extent of the Yokota et al. (2011) model and the shorter north-south (along-strike) extent of the Shao and Ji (2011) model. Also shown in Figure 3 are strong motion generation areas (SMGAs) presented by Kurahashi and Irikura (2011) and the high-frequency (0.5 Hz to 1 Hz) radiation areas evaluated from back-projection of teleseismic array observations by Meng et al. (2011). While these later studies do not provide resolution of the entire fault rupture process, they indicate regions where strong high-frequency energy was emitted and support the inclusion of relatively deep low-slip regions in the trimmed fault models.

Figure 4 plots cross sections of the three trimmed fault models as a function of distance perpendicular to strike, measured from the trench axis. The Wei et al. (2012) model uses a single fault plane, whereas Shao and Ji (2011) and Yokota et al. (2011) use three planes with fault dip increasing with depth. Also shown in Figure 4 is the subduction plate interface given by Miura et al. (2005). The single fault plane of Wei et al. (2012) is only able to closely match the plate interface in the middle portion of the fault. The Shao and Ji (2011) model is

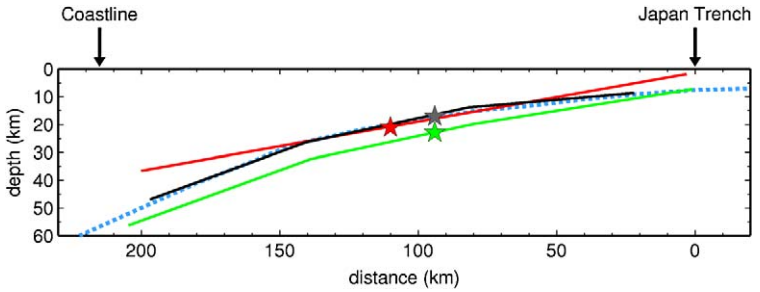

Figure 4. Depth cross section perpendicular to fault strike through the main shock hypocenter showing the geometry of the three trimmed fault models (Yokota = black, Shao = green, Wei = red). The colored stars indicate the hypocenter used for each model. Dashed blue line indicates the subducting plate interface from Miura et al. (2005). Locations of Japan Trench and coastline are also indicated.

Table 1. Yokota et al. (2011) fault plane segments

Top center[1] longitude	Top center[1] latitude	Strike (deg)	Dip (deg)	depth to top center[1] (km)	Along-strike length (km)	Down-dip width (km)
143.4464	37.4835	200	5	8.65	480	60
142.8276	37.6816	200	12	13.9	480	60
142.2021	37.8775	200	20	26.4	480	60

[1]Top center is the location of the midway point along the upper edge of each fault plane segment.

generally about 5 km to 8 km deeper than the Miura et al. (2005) plate interface, possibly due to their use of the JMA epicenter with a depth of 23 km. Wei et al. (2012) use the hypocenter determined by Chu et al. (2011), which is about 15 km west of the JMA epicenter and has a depth of 21 km. Chu et al. (2011) discuss the importance of hypocenter specification and its tradeoffs with fault geometry and its impact on the resolution of slip distribution for this earthquake. The Yokota et al. (2011) model used the JMA epicenter with a depth of 17 km and their fault geometry provides the closest match to the inferred plate interface.

Based on the above assessments, we have chosen to use the Yokota et al. (2011) fault representation for our distance measurements in the current study. Table 1 gives the locations and dimensions of the Yokota et al. (2011) fault plane segments.

GROUND MOTION DATABASE

GROUND MOTION NETWORKS

As described by Midorikawa et al. (2012), research ground motion networks that recorded the Tohoku-oki main shock include the K-NET and KiK-net maintained by the National Research Institute for Earth Science and Disaster Prevention (NIED), PARI-net operated by the Port and Airport Research Institute, and BRI-net operated by the Building Research Institute. Additional networks used for disaster management include the JMA-net operated by the Japan Meteorological Agency, various prefectures networks, and an MLIT network operated by the Ministry of Land, Infrastructure, and Transport.

In the present study, we utilized available data from the K-NET, KiK-net, PARI-net, and JMA-net arrays. The available data were reviewed to identify through visual inspection recordings for which all three components demonstrated a clear onset of shaking, so as to exclude from the data set records that may have had a P-trigger. This process yielded 1,238 triaxial accelerographs, most of which have locations shown in Figure 3. Further information on ground motion networks in Japan and recorded data from the Tohoku-oki main shock are provided by Midorikawa et al. (2012).

DATA PROCESSING

A total of 1,238 three-component, uncorrected digital accelerograms were selected as described above. Sponsored by the Pacific Earthquake Engineering Research (PEER) center, those motions were processed by Pacific Engineering and Analysis following PEER/NGA

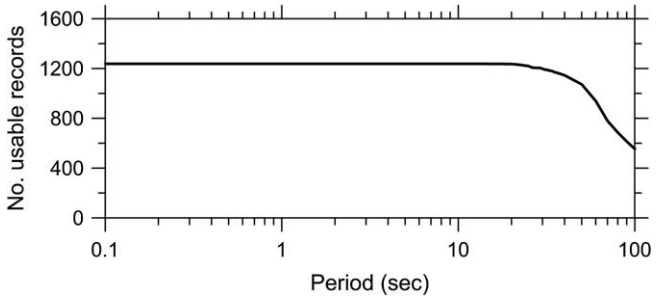

Figure 5. Number of usable two-component horizontal records as function of spectral period for the data set considered in this study.

protocols (Darragh et al. 2004, Chiou et al. 2008), which include selection of record-specific corner frequencies to optimize the usable frequency range. For KiK-net sites, only data from the ground surface stations are considered. The most important filter applied to the data is the low-cut filter, which removes low-frequency noise effects. We take the minimum usable frequency as $1.25 \times f_{HP}$, where f_{HP} is the high-pass (equivalent to low-cut) corner frequency used in the processing. Using the filtered records, we computed the intensity measures of peak acceleration (PGA), peak velocity (PGV), and pseudo-acceleration response spectra at a range of periods between 0.01 sec and 10.0 sec. Figure 5 presents the number of usable recordings as a function of period. A usable recording for period T is defined as having both horizontal components with $T < 1/(1.25 f_{HP})$. The data set is seen to fall off for periods beyond about 20 sec to 30 sec.

SITE CONDITIONS

The NIED website contains shear- and compression-wave velocity profiles for each of the K-NET and KiK-net sites except for five ocean-bottom sites. KiK-net profiles are always deeper than 30 m, whereas K-NET profiles are always 20 m or shallower. The measured shear wave velocity profiles were used to compute V_{S30} as follows:

1. When profile depth (z_p) is 30 m or greater (KiK-net sites), the V_s profile is used to compute V_{S30} as the ratio of 30 m to the shear wave travel time above a depth of 30 m.
2. When $z_p < 30$ m, compute V_{Sz} as the ratio of z_p to shear wave travel time from z_p to the ground surface.
3. When $z_p = 20$ m, compute V_{S30} from V_{Sz} and z_p using the correlation relationships originally developed for California by Boore (2004). When $z_p \leq 10$ m, compute V_{S30} from V_{Sz} and z_p using the correlation relationships developed from KiK-net data by Boore et al. (2011). For intermediate depths of $10 < z_p < 20$ m, interpolate between the above values.

The rationale behind Step (3) above is that shallow-depth K-NET profiles likely encountered firm geologic materials causing borehole drilling to stop. Firm geologic conditions are

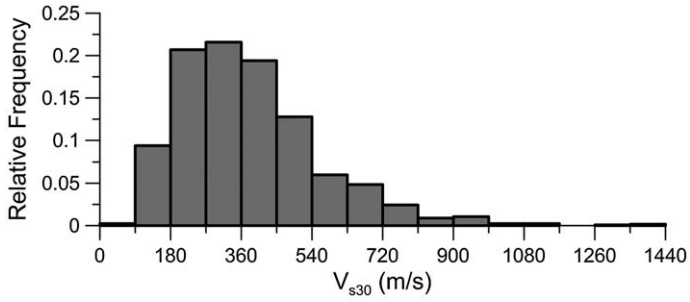

Figure 6. Histogram of V_{S30} values in data set.

also common for KiK-net sites. On the other hand, 20 m K-NET profiles are likely deeper sediments similar to the conditions prevalent in California. A histogram of V_{S30} values in the data set is shown in Figure 6. No velocity profiles are available for the five ocean-bottom sites and V_{S30} was assumed as 180 m/s for the present study.

For sites without velocity profiles, which includes all of the JMA-net and 9 of 20 PARI-net sites, we estimate V_{S30} using a proxy-based method described by Matsuoka et al. (2006). This method uses geomorphic and geologic conditions mapped across Japan (Wakamatsu and Matsuoka 2008) that are correlated by category to V_{S30}.

DISTANCE CALCULATION

We computed distances from each utilized recording station to the finite-fault rupture model shown in Figure 3 (and Table 1). The distance parameters that were computed are rupture distance (R_{rup}) and Joyner-Boore distance (R_{jb}), which is the closest distance to the surface projection of the rupture surface.

COMPARISONS TO GMPES

In this section, we compare the Tohoku-oki earthquake main shock data described in the previous section to several GMPEs using an approach, originally presented by Scasserra et al. (2009), in which specific attributes of the GMPE are examined relative to the data. In particular, we investigate the implications of the data for magnitude scaling, distance scaling, intra-event dispersion, and site effects. An alternative approach was presented by Scherbaum et al. (2004), in which overall goodness of fit of data to a model is computed by comparing normalized residuals to the standard normal variate. The selected approach was used because we seek the aforementioned physical insights provided by the ground motion data.

APPLICABLE MODELS

We utilize ground motion prediction equations (GMPEs) for interface subduction zone earthquakes by Atkinson and Boore (2003, 2008), Abrahamson et al. (2013), and Zhao et al. (2006), which we refer to subsequently as AB 2003, AEA 2013, and ZEA 2006, respectively. The first and third of these GMPEs were used to predict subduction zone ground motions in the USGS seismic hazard maps (Petersen et al. 2008). The AEA 2013 model has been

identified for use in subsequent versions of the USGS maps. We also consider a Japan-specific model by Si and Midorikawa (2000) that utilizes Japanese data from crustal, inter-plate, and intra-plate events. That model, which applies to PGA and PGV only, was selected due to its widespread usage in Japan, and it is denoted as SM 2000.

AB 2003 is based on worldwide subduction zone data and includes models specific to various regions of the world, including South America and Japan. The generic, non-regional version of the model is used here and the event terms are subsequently used to check the AB 2003 regional correction for Japan. We recognize that Atkinson and Macias (2009) have developed a subsequent GMPE for subduction regions, derived in part from simulations of large subduction earthquakes, which they recommend over AB 2003. The original AB 2003 model was selected due to its usage in numerous engineering applications (Petersen et al. 2008, Stewart et al. 2013). The largest magnitude in the AB data set is 8.3 and the largest well-recorded event is 8.0. ZEA 2006 and SM 2000 utilize data from worldwide crustal events, and they use Japanese data from multiple source types including interface and intra-slab subduction zone earthquakes. The AB and ZEA models apply to the geometric mean of the two horizontal components, whereas SM 2000 applies to the larger of two horizontal components. The developers of the AB, SM, and ZEA models each indicated their equations as applicable to an upper bound magnitude of 8.3. The AEA model is considered to be applicable to magnitude 9.0.

MAGNITUDE SCALING OF SPECTRAL ORDINATES

A key issue in ground motion prediction for interface subduction zone earthquakes is the functional form used for magnitude scaling. Many models produce essentially linear scaling of the logarithm of ground motion with magnitude (e.g., SM model in Figure 7 and a linear form of ZEA that is not used here), whereas others apply higher order terms that produce saturation of ground motion with increasing magnitude (e.g., AB 2003 and AEA 2013 models, as well as quadratic form of ZEA 2006 model in Figure 7). The SM 2000 model predictions shown in Figure 7 and elsewhere have been divided by 1.1 to correct from largest horizontal component to the geometric mean, based on the recommendations of Beyer and Bommer (2006).

In Figure 7, we plot ground motion intensity measures (IMs) at several spectral periods versus magnitude. The data are from AB 2003 (database available through an electronic supplement), the 2001 Southern Peru earthquake (Rodriguez-Marek et al. 2010), the Maule, Chile, earthquake (Boroschek et al. 2012), and Tohoku-oki earthquake. The data plotted have rupture distances between 70 km and 150 km and include all site conditions. The GMPE medians are for a distance of 100 km and an average site condition corresponding to $V_{S30} = 300$ m/s. The data for the Maule and Tohoku events appears to support saturation of ground motions at large magnitudes for the IMs considered, especially for high-frequency IMs.

DISTANCE SCALING AND RESIDUALS ANALYSIS

Figure 8a shows RotD50 values (i.e., median of single-azimuthal ground motions; Boore, 2010) for PGA, 0.1s, 1.0 s, and 3.0 s pseudo spectral accelerations (PSa) at 5% damping versus rupture distance. Data are shown for the following bins of V_{S30}: <200 m/s,

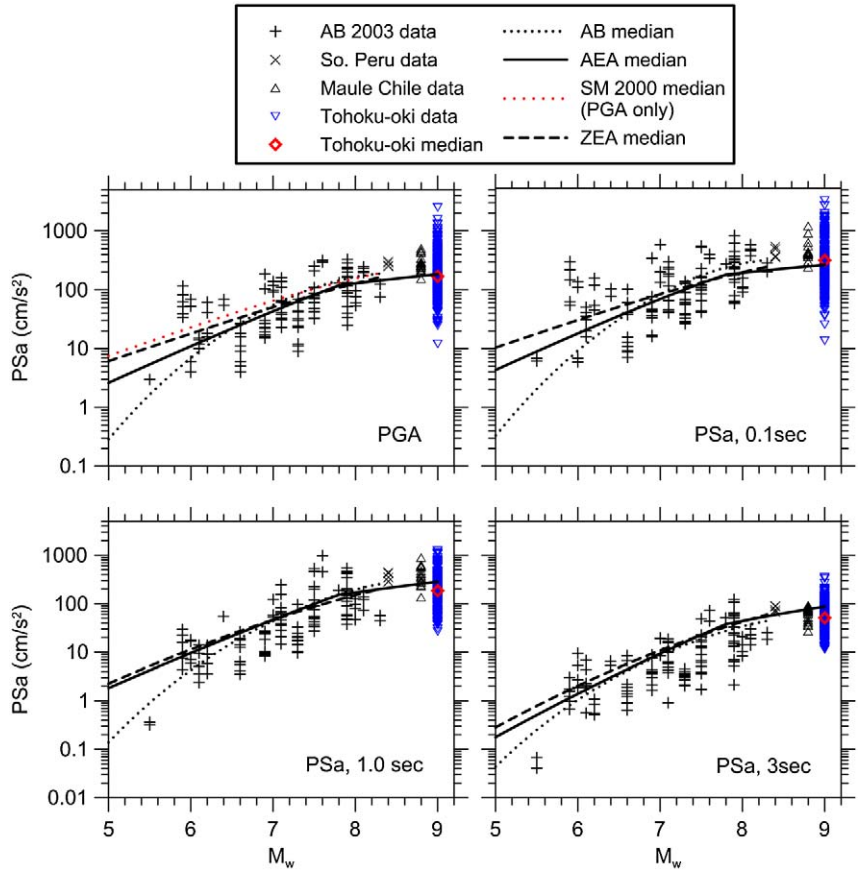

Figure 7. Scaling of spectral ordinates and PGA with magnitude from AB 2003 data set as well as Southern Peru, Maule (Chile) and Tohoku-oki earthquake data for distances between 70 km and 150 km. Median predictions from three GMPEs shown, which apply for reference soil conditions (approximate $V_{S30} = 300$ m/s) and distance of 100 km.

200–400 m/s, 400–760 m/s, and > 760 m/s. Also shown in Figure 8a are means and medians ± one within-event standard deviation (ϕ_{ln}) for the ZEA 2006 GMPE and medians for AB 2003 (without regional correction for Japan), AEA 2013 (for forearc and backarc regions) and SM 2000 (PGA only). The GMPEs are plotted for site categories corresponding to a reference condition of $V_{S30} = 300$ m/s. All of the GMPEs except AEA 2013 were extrapolated beyond the reported maximum usable magnitude for the present application.

Several significant trends are evident from Figure 8a. First, we see that the ZEA 2006, SM 2000, and AEA 2013 GMPEs have faster distance attenuation rates than AB 2003, and in addition, the data consistently attenuate faster with distance than predicted by AB 2003. ZEA 2006 appears to capture the distance attenuation rate at the two longer considered periods (1.0 and 3.0 sec), but it cannot capture the relatively fast attenuation of high-frequency parameters (0.1 sec PSa and PGA) beyond about 100 km. The SM 2000 trend for PGA is nearly identical

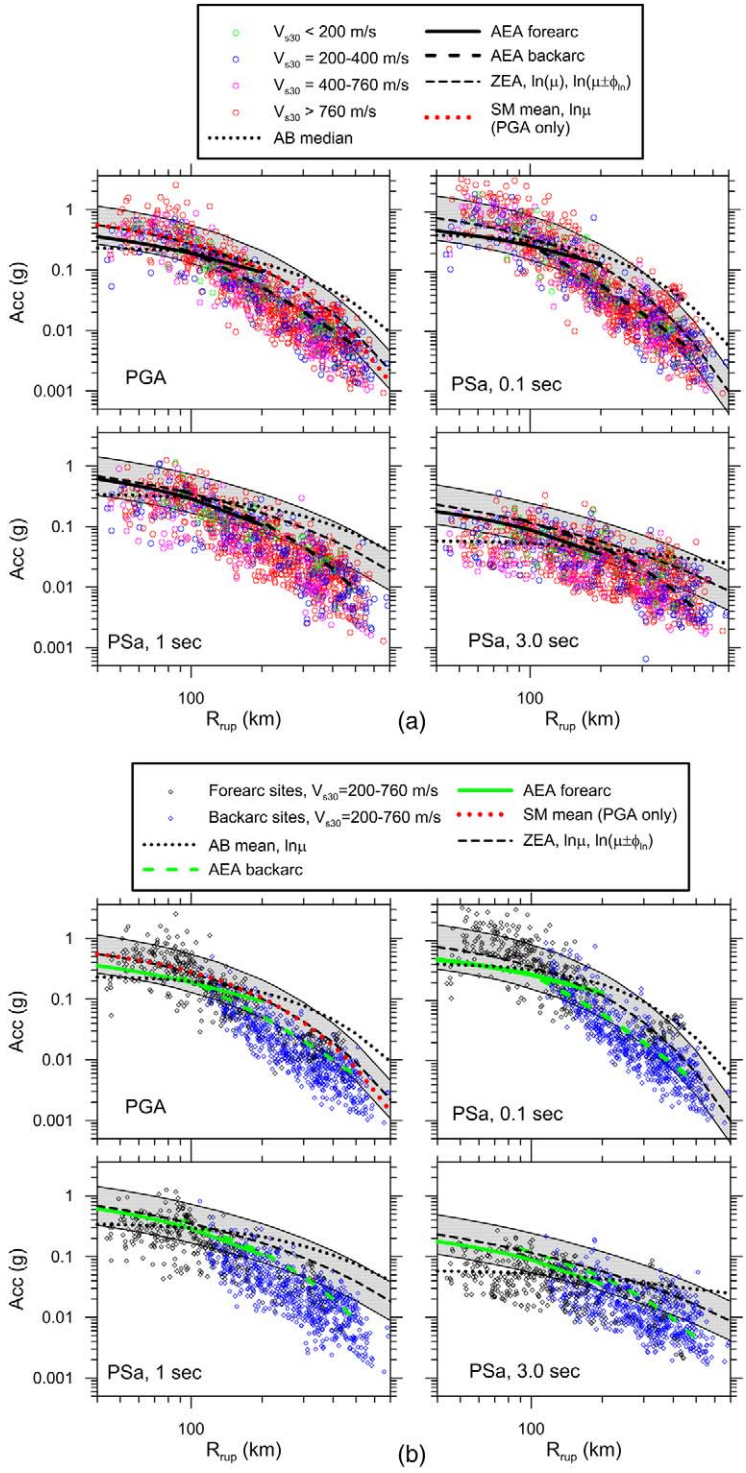

Figure 8. (a) Attenuation of PGA and spectral accelerations with distance and comparison to GMPEs for reference condition equivalent to $V_{S30} = 300$ m/s. For ZEA 2006 both the mean ($\ln \mu$) and mean ± one standard deviation ($\ln(\mu \pm \phi_{ln})$) are shown, whereas for AB 2003, AEA 2013, and SM 2000 only means are shown. The data are plotted as geometric means. ZEA 2006 applies to the geometric mean. AB 2003 applies to random component and no correction to the AB 2003 median has been applied. The SM 2000 median is divided by 1.1 to adjust from larger component to geometric mean per the recommendations of Beyer and Bommer (2006). (b) Same as Figure 8a except that data sorted into forearc and backarc sites and only data having $V_{S30} = 200 - 760$ m/s are shown.

to that of ZEA 2006. Average site effects are also evident from the data in Figure 8; soil sites (green and blue dots) are clearly higher on average than rock sites (purple and red dots) at the longer periods, but this trend does not hold for PGA or 0.1 sec PSa. Site effects are analyzed more formally in the following section.

Figure 8b shows the data from Figure 8a segregated into forearc and backarc regions according to the boundary in Figure 3. Data are shown only for intermediate site classes having $V_{S30} = 200 - 760$ m/s. The break in slope that occurs in the high-frequency data near $R_{rup} = 100 - 200$ km is seen to be the consequence of a transition from predominantly forearc to backarc sites. The relatively rapid attenuation in backarc regions is thought to result from increased anelastic attenuation (Ghofrani and Atkinson 2011). AEA 2012 is the only GMPE that incorporates the slope break associated with the forearc to backarc transition, and the backarc model does provide an improved fit, especially at short periods.

To more accurately evaluate the performance of the GMPEs, including corrections for site effects, we calculate total residuals (including inter- and intra-event components; see, for example, Scasserra et al. 2009 for further explanation of the methodology) for each data point considering the appropriate source distance and site condition as follows:

$$R_i = \ln(IM_i)_{rec} - (\mu_i)_{GMPE} \tag{1}$$

where $(IM_i)_{rec}$ = value of ground motion intensity measure from recording i and $(\mu_i)_{GMPE}$ = mean value of that same IM (in natural log units) from the GMPEs. Residuals in forearc and backarc regions are plotted versus distance in Figure 9 along with running means for distance bins. In forearc regions, the AEA 2013 residuals show a generally flat trend for distances up to approximately 150–200 km. At high frequencies, forearc residuals for all three GMPEs trend downward beyond approximately 150–200 km and then trend sharply upward beyond approximately 250 km. The sites producing the upward trend are principally on the southeast (forearc) side of Hokkaido. We do not know what feature of the crustal structure in this region might be responsible for this trend, although high Q (low crustal damping) has been noted in this region by Hashida (1987). The downward trends of high-frequency forearc residuals for models AB and ZEA extend to close distances (approximately 50 km). At periods of 1.0 and 3.0 sec, the forearc residual trends are quite different among the three models, with AB trending strongly downward, AEA 2013 trending upward, and ZEA 2006 being relatively flat.

The backarc region, which begins at approximately 110 km, has high-frequency residuals that trend downward to at least 300 km, especially for AB 2003 and ZEA 2006. This trend flattens or reverses beyond approximately 200 km (for AEA 2012) and 300 km (for AB 2003 and ZEA 2006). At longer periods, the backarc residuals follow generally similar trends to those in the forearc region, which is expected because the different anelastic attenuation of backarc regions has less effect for long-period ground motion components. The general trends we have noted regarding the misfit of models to data at large distance is consistent with observations from prior studies (e.g., Furumura et al. 2011, Skarlatoudis and Papazachos 2012, and Midorikawa et al. 2012). The relatively strong distance attenuation in backarc regions has been noted previously by Ghofrani and Atkinson (2011) and Skarlatoudis and Papazachos (2012).

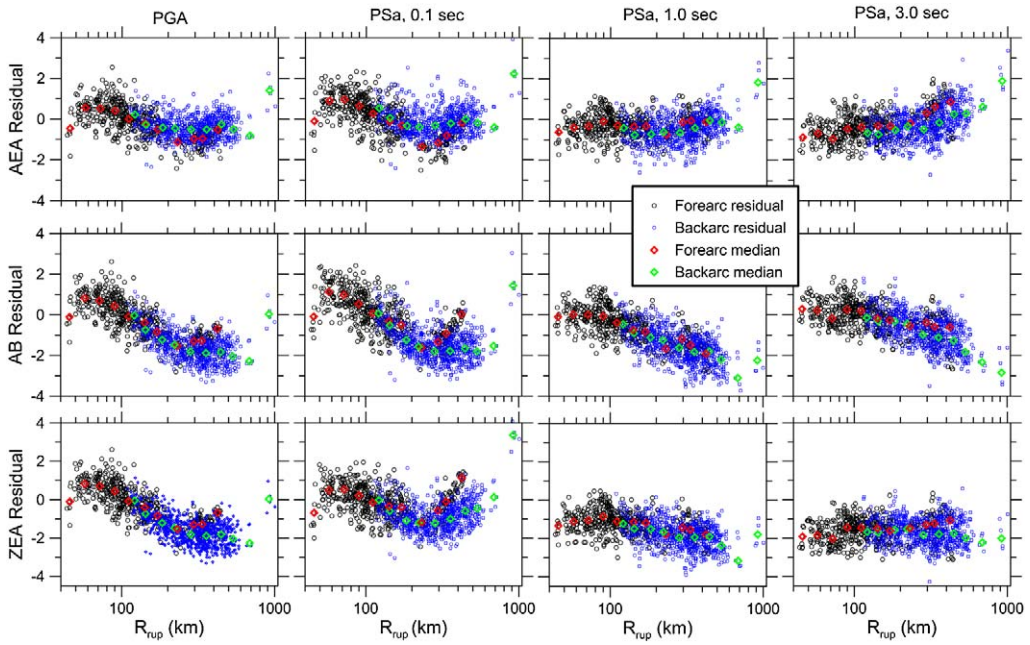

Figure 9. Total residuals of Tohoku-oki recordings within forearc and backarc regions relative to AB 2003, AEA 2012, and ZEA 2006 GMPEs along with mean residuals within distance bins.

As shown in Figure 9, in most cases, the data clouds are not centered at zero ordinate, indicating systematic misfits of the GMPEs relative to the data. Since the event is very well recorded, this bias is practically equivalent to an event term as would be calculated from a mixed-effects regression (e.g., Abrahamson and Youngs 1992). Non-zero event terms (η) are typical; what is of interest is to see if the Tohoku-oki event terms are consistent with event-to-event scatter (represented by event term dispersion τ) and regional trends of GMPE bias as observed from previous earthquakes. Figure 10 shows event terms, calculated as the median residual within 100 km, for the AB 2003, AEA 2013, and ZEA 2006 GMPEs as a function of spectral period along with the $\pm\tau$ model (inter-event standard deviation) from AB 2003. We only use residuals within 100 km because of the aforementioned distance attenuation misfits, which should not be mapped into event terms. The event terms peak at about 0.1 sec and decrease at longer periods. The AB 2003 event terms follow closely the Japan region bias reported by AB 2003 (their Table 3), indicating that the misfit of the Tohoku-oki data relative to the AB 2003 model is consistent with previous data from Japan used in the development of the AB 2003 GMPE.

Event-specific within-event standard deviations in natural log units (denoted as ϕ_{ln}) can be calculated as the standard deviation of residuals from Equation 1. We compute this dispersion using residuals for all distances. Because the GMPE and data attenuation rates are significantly different, especially at short periods, the ϕ_{ln} values computed from data are higher than those from the GMPEs. Figure 11 shows that standard deviations for AEA 2013 and ZEA 2006 are substantially lower than those from AB 2003 at short periods,

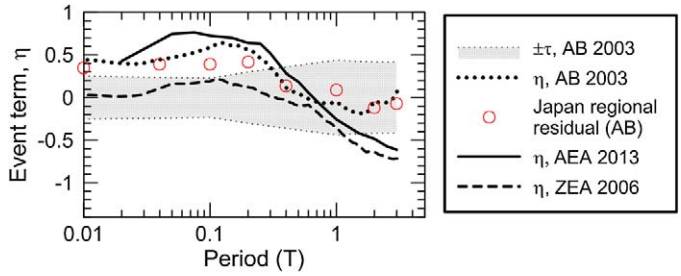

Figure 10. Estimated event terms of Tohoku-oki main shock relative to the AB 2003, AEA 2013, and ZEA 2006 GMPEs. Also shown is the AB inter-event standard deviation (τ) and the AB regional model bias for Japan (red circles). Estimated event terms were computed using data with $R_{rup} < 100$ km.

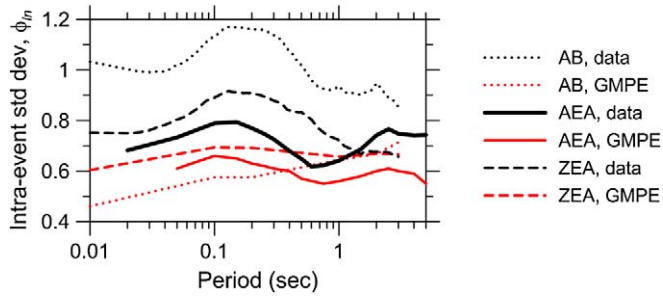

Figure 11. Intra-event standard deviation for Tohoku-oki earthquake data as compared to the AB 2003, AEA 2012, and ZEA 2006 intra-event standard deviations, ϕ_{ln}. Dispersion computed using data over all distances.

which is due to more accurate distance attenuation. At long periods, dispersion levels for AEA 2012 and ZEA 2006 residuals fall to levels near those from the GMPEs.

SITE EFFECTS

In this section, we present a preliminary evaluation of site amplification, specifically in reference to the scaling of ground motions with V_{S30}. As of this writing, we have not formally investigated higher-order effects such as nonlinearity in site response, which will be the subject of future work.

To evaluate site amplification, we utilize a non-reference site approach in which residuals are calculated between data and a GMPE applied for reference rock site conditions as follows:

$$R_i^r = \ln(IM_i)_{rec} - ((\mu_i^r)_{GMPE} + \eta) \tag{2}$$

where R_i^r indicates the residual of recording i from a rock GMPE, μ_i^r is a rock GMPE mean (in natural log units) for the magnitude and distance corresponding to recording i, and η is the event term appropriate for the earthquake event and IM. The reference site condition is

taken as reference rock for AB 2003 (their site parameters S_C, S_D, and S_E are set to zero), $V_{S30} = 1{,}100$ m/s for AEA 2013, and hard rock for ZEA 2006 (equivalent to NEHRP site category A).

A meaningful analysis of site effects from the Tohoku data set is complicated by the significant distance attenuation misfits identified in the previous section, which cause large non-zero residuals for reasons unrelated to site response. Accordingly, for the analysis of site effects, we use a subset of the data from forearc sites at rupture distances $R_{rup} < 200$ km, for which distance attenuation trends are relatively well-matched by the GMPEs. Figure 12 shows the trends of AEA 2013 reference site residuals against V_{S30} for the intensity measures of PGA and PSa at 0.1 sec, 1.0 sec, and 3.0 sec. A log-linear regression using all data is also shown along with its 95% confidence intervals. Figure 13 shows the slopes of these fit lines (denoted as c) for the three models as a function of period, which are seen to be similar. Also shown in Figure 13 for reference purposes are similarly computed slopes applicable to active crustal regions (ACRs), which were mostly from California (Choi and Stewart 2005).

The most important observation from the data trends in Figure 12 is the trend (or lack thereof) of reference site residuals with increasing V_{S30}. Low-frequency ground motions show a statistically significant trend as indicated by the negative slope of the fit line ($c < 0$), whereas high-frequency ground motions have a nearly zero, or even positive, slope. As shown in Figure 13, these slopes are different from the average for active crustal regions (ACRs) evaluated by Choi and Stewart (2005), which are significantly negative at low and high frequencies. These differences are of considerable practical importance, as it suggests that the scaling of ground motions with V_{S30} may be region-dependent. Although

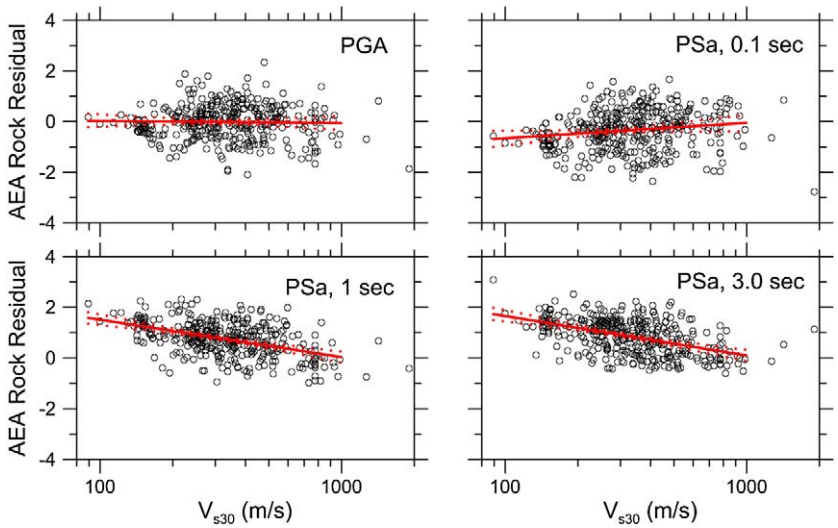

Figure 12. Reference rock residuals of Tohoku-oki recordings using AEA 2013 GMPE for rock site conditions. Residuals shown for forearc data with $R_{rup} < 200$ km along with linear regression fit and confidence intervals.

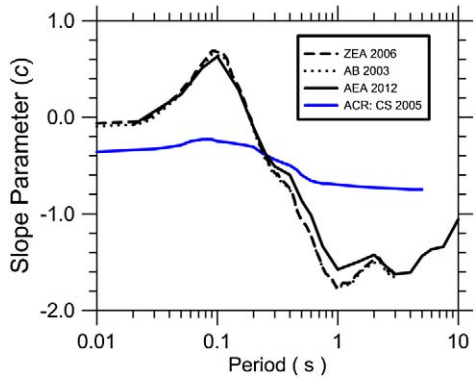

Figure 13. V_{S30}-scaling of reference rock residuals from Tohoku-oki recordings (c parameter) along with comparable values for data from active crustal regions (Choi and Stewart 2005).

unpublished as of this writing, similar findings have been found in the NGA-West 2 project through a similar (i.e., with distance cut-off) examination of an extensive set of ACR data. Regional variations in site response have been observed in previous research, although not (to our knowledge) in the form of regionally variable V_{S30}-scaling relationships. Atkinson and Casey (2003) computed different site responses using quarter-wavelength theory for Japan and the Pacific Northwest, which explained regional differences in ground motions. Moreover, Oth et al. (2011) and Ghofrani et al. (2013) have observed site response features in Japan, including significant high-frequency amplification, which is seldom encountered in other active regions, such as California.

We note that the data for high-frequency IMs in Figure 12 show principally negative residuals between $V_{S30} \approx 130$ m/s and 200 m/s, which has been observed previously from Japanese data by the last author (KWC). It is not known whether this trend is sufficiently robust to support the use of a nonlinear V_{S30}-scaling relationship.

SUMMARY AND CONCLUSIONS

The Tohoku-oki event is the largest-magnitude earthquake to produce usable recordings. In combination with the data from the 2010 Maule, Chile, earthquake (Boroschek et al. 2012), the data can be used to evaluate magnitude scaling of various ground motion intensity measures (IMs), which has generally been represented with linear or quadratic functions in recent GMPEs for subduction zone interface earthquakes. The data support saturation of the logarithm of IMs with increasing magnitude for the IMs considered, especially at high frequencies, indicating that linear magnitude scaling should not be used for large magnitudes.

The data demonstrate a scaling with distance that is demonstrably faster in backarc than forearc regions for high-frequency IMs. In both forearc and backarc regions, the AEA 2013 model best captures the high-frequency distance attenuation trends. All of the models underpredict the attenuation rate in backarc regions for high-frequency IMs for rupture distances under about 200 km to 300 km. Distance attenuation misfits are mixed among the three models at long periods, being too-fast for AEA 2013, too-slow for AB 2003, and about right for ZEA 2006. The high-frequency distance attenuation trends are different from

those from the Maule event (Boroschek et al. 2012), where distance attenuation rates were slower and were well captured by the AB 2003 model and overpredicted by the ZEA 2006 model.

Using a non-reference site approach, we find that the scaling of site amplification with V_{S30} is weak to nonexistent for high-frequency ground motions, but strong for low frequencies. Given the well-established and significant scaling of site amplification at low and high frequencies observed elsewhere (principally California), these findings suggest that the V_{S30} scaling of ground motions may have regional dependence. This is not particularly surprising given that V_{S30} is a proxy for geologic structure, and since geologic conditions are regionally variable (e.g., Atkinson and Casey 2003), the scaling of ground motion with V_{S30} can therefore also be expected to be region-dependent. Similar findings (unpublished) are also emerging from analysis of shallow crustal earthquake data in the NGA-West 2 project, indicating that this trend is not confined to this single earthquake.

We evaluate event terms using recordings within rupture distances of 100 km because the problems with distance attenuation become particularly pronounced beyond that distance. Event terms are generally positive (indicating underprediction) for periods less than 0.7 sec to 1.0 sec and peak at about 0.1 sec to 0.2 sec. At periods longer than about 1.0 sec, the AB event terms are nearly zero, whereas AEA 2013 and ZEA 2006 event terms are negative. The AB 2003 event terms follow quite well the regional bias for Japan presented by AB 2003 with their Japan-specific regional correction factor.

Within-event dispersion levels are higher than those from the corresponding GMPEs at high frequencies due to the distance attenuation misfits. The AEA 2013 and ZEA 2006 models have the lowest high-frequency dispersion levels among the three models. AB 2003 residuals have the highest dispersion due to the relatively large distance attenuation misfit. At long periods, dispersion levels for the AEA 2013 and ZEA 2006 residuals fall to levels near those from the corresponding GMPEs.

ACKNOWLEDGEMENTS

The participation of the first author in reconnaissance activities for this earthquake was supported by the Geotechnical Extreme Events Reconnaissance (GEER) Association, which receives financial support from the National Science Foundation. Partial support from the USGS, through NEHRP funding to PEER, is gratefully acknowledged. We thank Elizabeth Cochran, Paul Spudich, Gail Atkinson, and two anonymous reviewers for their helpful and insightful reviews of this manuscript, which have improved the final product.

REFERENCES

Abrahamson, N. A., and Youngs, R. R., 1992. A stable algorithm for regression analyses using the random effects model, *Bull. Seism. Soc. Am.* **82**, 505–510.

Abrahamson, N. A., Gregor, N., and Addo, K., 2012. BCHydro ground motion prediction equations for subduction earthquakes, *Earthquake Spectra*, submitted.

Ammon, C. J., Lay, T., Kanamori, H., and Cleveland, M., 2011. A rupture model of the 2011 off the Pacific coast of Tohoku Earthquake, *Earth Planets Space* **63**, 693–696.

Atkinson, G. M., and Boore, D. M., 2003. Empirical ground-motion relations for subduction-zone earthquakes and their application to Cascadia and other regions, *Bull. Seism. Soc. Am.* **93**, 1703–1729.

Atkinson, G. M., and Boore, D. M., 2008. Erratum to empirical ground-motion relations for subduction zone earthquakes and their application to Cascadia and other regions, *Bull. Seism. Soc. Am.* **98**, 2567–2569.

Beyer, K., and Bommer, J. J., 2006. Relationships between median values and between aleatory variabilities for different definitions of the horizontal component of motion, *Bull Seism Soc Am.* **96**, 1512–1522.

Boore, D. M., 2010. Orientation-independent, nongeometric-mean measures of seismic intensity from two horizontal components of motion, *Bull. Seism. Soc. Am.* **100**, 1830–1835.

Boore, D. M., 2004. Estimating V_{S30} (or NEHRP site classes) from shallow velocity models (depth < 30 m), *Bull. Seism. Soc. Am.* **94**, 591–597.

Boore, D. M., Thompson, E. M., and Cadet, H., 2011. Regional correlations of V_{S30} and velocities averaged over depths less than and greater than 30 m, *Bull. Seism. Soc. Am.* **101**, 3046–3059.

Boroschek, R., Contreras, V., Kwak, D. Y., and Stewart, J. P., 2012. Strong ground motion attributes of the 2010 M_w 8.8 Maule Chile Earthquake, *Earthquake Spectra* **28**, S19–S38.

Chiou, B. S.-J., Darragh, R., Dregor, D., and Silva, W. J., 2008. NGA project strong-motion database, *Earthquake Spectra* **24**, 23–44.

Choi, Y., and Stewart, J. P., 2005. Nonlinear site amplification as function of 30 m shear wave velocity, *Earthquake Spectra* **21**, 1–30.

Chu, R. S., Wei, S., Helmberger, D., Kanamori, H., Zhan, Z. W., and Zhu, L. P., 2011. Beginning of the great M_w = 9.0 Tohoku-Oki earthquake, *Earth and Planetary Sciences Letters* **308**, 277–283.

Cox, B. R., Boulanger, R. W., Tokimatsu, K., Wood, C., Abe, A., Ashford, S. A., Donahue, J., Ishihara, K., Kayen, R. E., Katsumata, K., Kishida, T., Kokusho, T., Mason, H. B., Moss, R. E. S., Stewart, J. P., Tohyama, K., and Zekkos, D., 2013. Liquefaction at strong motion stations in Urayasu City during the 2011 Tohoku-oki earthquake, *Earthquake Spectra* **29**, S55–S80.

Darragh, R., Silva, W. J., and Gregor, N., 2004. Strong motion record processing for the PEER center, *Proc. Workshop on Strong Motion Record Processing*, Richmond, CA, 26–27 May 2004, available at http://www.cosmos-eq.org/recordProcessingPapers.html.

Furumura, T., Takemura, S., Noguchi, S., Takemoto, T., Maeda, T., Iwai, K., and Pdhy, S., 2011. Strong ground motions from the 2011 off-the Pacific-Coast-of-Tohoku, Japan (M_w = 9.0) earthquake obtained from a dense nationwide seismic network, *Landslides* **8**, 333–338.

Geological Survey of Japan, 1992. Geological Map of Japan, Third Edition, CD-ROM version, 1:1,000,000.

Geospatial Information Authority of Japan, 1997. *The National Atlas of Japan* (CD-ROM).

Ghofrani, H., and Atkinson, G. M., 2011. Forearc versus backarc attenuation of earthquake ground motion, *Bull. Seism. Soc. Am.* **101**, 3032–3045.

Ghofrani, H., Atkinson, GM., and Goda., K, 2012. Implications of the 2011 M9.0 Tohoku Japan earthquake for the treatment of site effects in large earthquakes, *Bull. Eqk. Eng.* **11**, 171–203.

Hashida, T., 1987. Determination of three-dimensional attenuation structure and source acceleration by inversion of seismic intensity data: Japanese islands, *Bull. Earthquake Research Institute, University of Tokyo*, **62**, 247–287.

Japan Metrological Agency (JMA), 2012. *Centroid Moment Tensor (CMT) Solutions*, available at http://www.seisvol.kishou.go.jp/eq/mech/cmt/cmt201103.html (last accessed March 2012).

Kawashima, K., and Buckle, I., 2013. Structural performance of bridges in the 2011 Tohoku-oki earthquake, *Earthquake Spectra* **29**, S315–S338.

Koketsu, K., Yokota, Y., Nishimura, N., Yagi, Y., Miyazaki, S., Satake, K., Fujii, Y., Miyake, H., Sakai, S., Yamanaka, Y., and Okada, T., 2011. A unified source model for the 2011 Tohoku earthquake, *Earth and Planetary Science Letters* **310**, 480–478.

Kurahashi, S., and Irikura, K., 2011. Source model for generating strong ground motions during the 2011 off the Pacific coast of Tohoku Earthquake, *Earth Planets Space* **63**, 571–576.

Lee, S. J., Huang, B. S., Ando, M., Chiu, H. C., and Wang, J. H., 2011. Evidence of large scale repeating slip during the 2011 Tohoku-Oki earthquake, *Geophys. Res. Lett.* **38**, No. 19, L19306, doi:10.1029/2011GL049580.

Matsuoka, M., Wakamatsu, K., Fujimoto, F., and Midorikawa, S., 2006. Average shear-wave velocity mapping using Japan engineering geomorphologic classification map, *Journal of Structural Mechanics and Earthquake Engineering* **23**, 57s–68s.

Meng, L. S., Inbal, A., and Ampuero, J. P., 2011. A window into the complexity of the dynamic rupture of the 2011 Mw 9 Tohoku-Oki earthquake, *Geophys. Res. Lett.* **38**, L00G07, doi:10.1029/2011GL048118.

Midorikawa, S., Miura, H., and Atsumi, T., 2012. Strong ground motion during the 2011 Off the Pacific Coast of Tohoku earthquake, *Proc. 9th Int. Conf. on Urban Earthquake Eng. & 4th Asia Conf. on Earthquake Eng.*, 6–8 March 2012, Tokyo Institute of Technology, Tokyo, Japan.

Miura, S., Takahashi, N., Nakanishi, A., Tsuru, T., Kodaira, S., and Kaneda, Y., 2005. Structural characteristics off Miyagi forearc region, the Japan Trench seismogenic zone, deduced from a wide-angle reflection and refraction study, *Tectonophysics* **407**, 165–188.

Mori, N., Cox, D. T., Yasuda, T., and Mase, H., 2013. Overview of the 2011 Tohoku earthquake tsunami damage in relation to coastal protection along the Sanriku Coast, *Earthquake Spectra* **29**, S127–S143.

Okazaki, T., Lignos, D. G., Midorikawa, M., Ricles, J. M., and Love, J., 2013. Damage to steel buildings observed after the 2011 Tohoku-oki earthquake, *Earthquake Spectra* **29**, S219–S243.

Oth, A., Bindi, D., Parolai, S., and Di Giacomo, D., 2011. Spectral analysis of K-NET and KiK-net data in Japan, Part II: On attenuation characteristics, source spectra, and site response of borehole and surface stations, *Bull. Seism. Soc. Am.* **101**, 667–687.

Petersen, M. D., Frankel, A. D., Harmsen, S. C., Mueller, C. S., Haller, K. M., Wheeler, R. L., Wesson, R. L., Zeng, Y., Boyd, O. S., Perkins, D. M., Luco, N., Field, E. H., Wills, C. J., and Rukstales, K. S., 2008. *Documentation for the 2008 Update of the United States National Seismic Hazard Maps*, Open-File Report 2008–1128, U.S. Geological Survey.

Rodriguez-Marek, A., Bay, J. A., Park, K., Montalva, G. A., Cortez-Flores, A., Wartman, J., and Boroschek, R., 2010. Engineering analysis of ground motion records from the 2001 M_w8.4 Southern Peru earthquake, *Earthquake Spectra* **26**, 499–524.

Scasserra, G., Stewart, J. P., Bazzurro, P., Lanzo, G., and Mollaioli, F., 2009. A comparison of NGA ground motion prediction equations to Italian data, *Bull. Seism. Soc. Am.* **99**, 2961–2978.

Scherbaum, F., Cotton, F., and Smit, P., 2004. On the use of response spectral reference data for the selection and ranking of ground motion models for seismic hazard analysis in regions of moderate seismicity: The case of rock motion, *Bull. Seism. Soc. Am.* **94**, 2164–2185.

Shao, G., and Ji, C., 2011, Rupture characterizations of the 2011 Mw 9.1 off the Pacific coast of Tohoku earthquake and its March 9th M_w 7.4 foreshock constrained by an unprecedented data

set for subduction earthquakes, Abstract U34A-03 presented at *2011 Fall Meeting, AGU*, San Francisco, CA.

Si, H., and Midorikawa, S., 2000. New attenuation relations for peak ground acceleration and velocity considering effects of fault type and site condition, *Proc. World Conf. Earthquake Eng.*, Auckland, NZ, Paper 0532.

Simons, M., Minson, S. E., Sladen, A., Ortega, F., Jiang, J. L., Owen, S., Meng, L. S., Ampuero, J. P., Wei, S. J., Chu, R. S., Helmberger, D. V., Kanamori, H., Hetland, E., Moore, A. W., and Webb, F. H., 2011. The 2011 magnitude 9.0 Tohoku-oki earthquake: Mosaicking the megathrust from seconds to centuries, *Science* **332**, 1421–1425.

Skarlatoudis, A., and Papazachos, C. B., 2012. Preliminary study of the strong ground motions of the Tohoku, Japan, earthquake of 11 March 2011: Assessing the influence of anelastic attenuation and rupture directivity, *Seism. Research Ltrs.* **83**, 119–129.

Stewart, J. P., Douglas, J., Javanbarg, M. B., Di Alessandro, C., Bozorgnia, Y., Abrahamson, N. A., Boore, D. M., Campbell, K. W., Delavaud, E., Erdik, M., and Stafford, P. J., 2013. Selection of ground motion prediction equations for the Global Earthquake Model, *Earthquake Spectra*, accepted, DOI: 10.1193/013013EQS017M.

Wakamatsu, K., and Matsuoka, M., 2008. Development of national topography and site condition map with 250-m mesh size, *Annual Meeting of Japan Association for Earthquake Engineering, 2008.11*, 222–223 (in Japanese).

Wei, S., Graves, R., Helmberger, D., Avouac, J. P., and Jiang, J., 2012. Sources of shaking and flooding during the Tohoku-Oki Earthquake: a mixture of rupture styles, *Earth Planet. Sci. Lett.*, in press.

Yokota, Y., Koketsu, K., Fujii, Y., Satake, K., Sakai, S., Shinohara, M., and Kanazawa, T., 2011. Joint inversion of strong motion, teleseismic, geodetic, and tsunami data sets for the rupture process of the 2011 Tohoku earthquake, *Geophys. Res. Lett.* **38**, L00G21, doi:10.1029/2011GL050098.

Zhao, J. X., 2011. Personal communication.

Zhao, J. X., Zhang, J., Asano, A., Ohno, Y., Oouchi, T., Takahashi, T., Ogawa, H., Irikura, K., Thio, H. K., Somerville, P. G., Fukushima, Y., and Fukushima, Y., 2006. Attenuation relations of strong ground motion in Japan using site classification based on predominant period, *Bull. Seismol. Soc. Am.* **96**, 898–913.

(Received 1 April 2012; accepted 30 November 2012)

2 Comparison of 2011 Tohoku-oki Mainshock and Two Subsequent Events

The Mw 9.0 Tohoku-oki Japan earthquake produced many subsequent aftershocks and triggered events. These events were very well recorded, providing an opportunity for a detailed study of source, path, and site effects. We processed Tohoku's seven foreshocks and 52 aftershocks for the NGA-Sub database. In this study, we consider two subsequent events, one Mw 6.7 on the plate interface, and another Mw 6.3 event located inland from the volcanic front (crustal event). For the these crustal and interface events, we respectively processed 554 and 641 three-component accelerograms, by applying component-specific low- and high-cut filters for, respectively. Usable response spectral periods are from 0.01 sec to 10-30 sec for both events. The recordings have rupture distances between 10 km and 400 km, and 60 km and 700 km for crustal and interface events, respectively. The ground motion characteristics of these two events and the Tohoku mainshock are compared. By using these data, we also evaluated the existing ground motion prediction equations (GMPEs). The results are presented in a paper entitled "*Comparison of Ground Motion Attributes from 2011 Tohoku-oki Mainshock and Two Subsequent Events*" by Kishida, T., Stewart, J. P., Graves, R. W., Midorikawa, S., Miura, H., Bozorgnia, Y. and Campbell, K. W., published in the Proceedings of the 10th International Conference on Urban Earthquake Engineering, CUEE (2013), Japan. The paper is presented in the following section.

10CUEE CONFERENCE PROCEEDINGS
10th International Conference on Urban Earthquake Engineering
March 1-2, 2013, Tokyo Institute of Technology, Tokyo, Japan

COMPARISON OF GROUND MOTION ATTRIBUTES FROM 2011 TOHOKU-OKI MAINSHOCK AND TWO SUBSEQUENT EVENTS

Tadahiro Kishida[1)], Jonathan P. Stewart[2)], Robert W. Graves[3)], Saburoh Midorikawa[4)], Hiroyuki Miura[5)], Yousef Bozorgnia[1)] , and Kenneth W. Campbell[6)]

1) Post-Doctoral Scholar (TK) and Executive Director (YB), Pacific Earthquake Engineering Research Center, Berkeley, CA, USA
2) Professor and Chair, Dept. of Civil & Environmental Engineering, Univ. of California, Los Angeles, CA, USA
3) Seismologist, US Geological Survey, Pasadena, CA, USA
4) Professor, Tokyo Institute of Technology, Japan
5) Associate Professor, Hiroshima University, Japan
6) Vice President, EQECAT Inc, Beaverton OR, USA

tkishida@berkeley.edu, jstewart@seas.ucla.edu, rwgraves@usgs.gov, ,
smidorik@enveng.titech.ac.jp, hmiura@hiroshima-u.ac.jp, yousef@berkeley.edu, kcampbell@eqecat.com

Abstract: The M_w 9.0 Tohoku-oki Japan earthquake and many of its subsequent aftershocks and triggered events were very well recorded, providing opportunity for detailed study of source, path, and site effects. In previous work, we utilized mainshock data to demonstrate faster attenuation with distance in backarc than in forearc regions, positive event terms for high frequency intensity measures for multiple ground motion prediction models, and minimal scaling of site amplification with V_{s30} at high frequencies. In this paper, we consider two subsequent events, one M_w 6.7 on the plate interface that ruptured in the mainshock and one M_w 6.3 inland from the volcanic front, to examine if similar ground motion features are apparent from these data sets. We continue to find evidence for the divergence in attenuation rate in forearc and backarc regions, despite the fact that the events are located on opposite sides of the volcanic front. The site response for these events does not appear to follow previously observed patterns for Japan, being relatively similar to V_{s30}-scaling in active crustal regions generally.

1. INTRODUCTION

The M_w 9.0 Tohoku-oki earthquake occurred on March 11 2011 along the plate boundary off the Pacific Coast of Japan. In prior work (Stewart et al., 2013), we reviewed the mainshock source solutions and selected a representative source model for engineering application; we described the uniform ground motion processing applied to approximately 2000 available triaxial accelerograms; and we described the results of data analysis to investigate source, path and site effects. For short period ground motion intensity measures, we found faster attenuation with distance in backarc than in forearc regions, positive event terms for multiple ground motion prediction models at short periods, and minimal scaling of site amplification with V_{s30}. Many of these effects disappeared at long periods.

Many of these observations are of substantial practical significance for ground motion prediction, and therefore there is interest in seeing if they are repeatable. This paper represents a first step in this direction. We select two well recorded events that occurred subsequent to the mainshock, one M_w 6.7 on the same plate interface that ruptured in the mainshock and one M_w 6.3 inland from the volcanic front. Identical data processing procedures are applied to these recordings as were used for the mainshock. Our objective is to see if similar ground motion features are apparent from these data sets as were found from the mainshock.

2. SELECTED EVENTS AND AVAILABLE DATA

We selected two events from the Japan Meteorological Assoc. (JMA) web site (http://www.seisvol.kishou.go.jp/eq/sourceprocess/). Attributes of the two events are given in Table 1. We refer to the 12 March 2011 event as 'crustal' and the 23 June 2011 event as 'interface.' As shown in Figure 1, the crustal event occurred in the backarc region. It had a reverse-slip mechanism and a shallow focal depth (8 km). The interface event occurred near the northwest corner of the mainshock fault plane (Fig. 1). It had a reverse-slip mechanism along a 17 deg. westward dipping fault plane and a focal depth of 36 km, which are consistent with rupture along the plate interface. In addition, this event is located close to the 03-11-2011 M_w 7.4 aftershock (Fig 1), which is also inferred to have rupture at the plate interface.

Table 1. Attributes of selected events

Date	M_w	Top-Ctr Lat, Long	Depth to top (km)	Length, width (km)	Strike / dip (°)
3/2011	6.3	37.051, 138.532	4.4	12, 12	26 / 32
6/2011	6.7	39.982, 142.588	36	18, 12	185/17

There are hundreds of well recorded events following the Tohoku mainshock. Our reasons for selecting these specific events were:

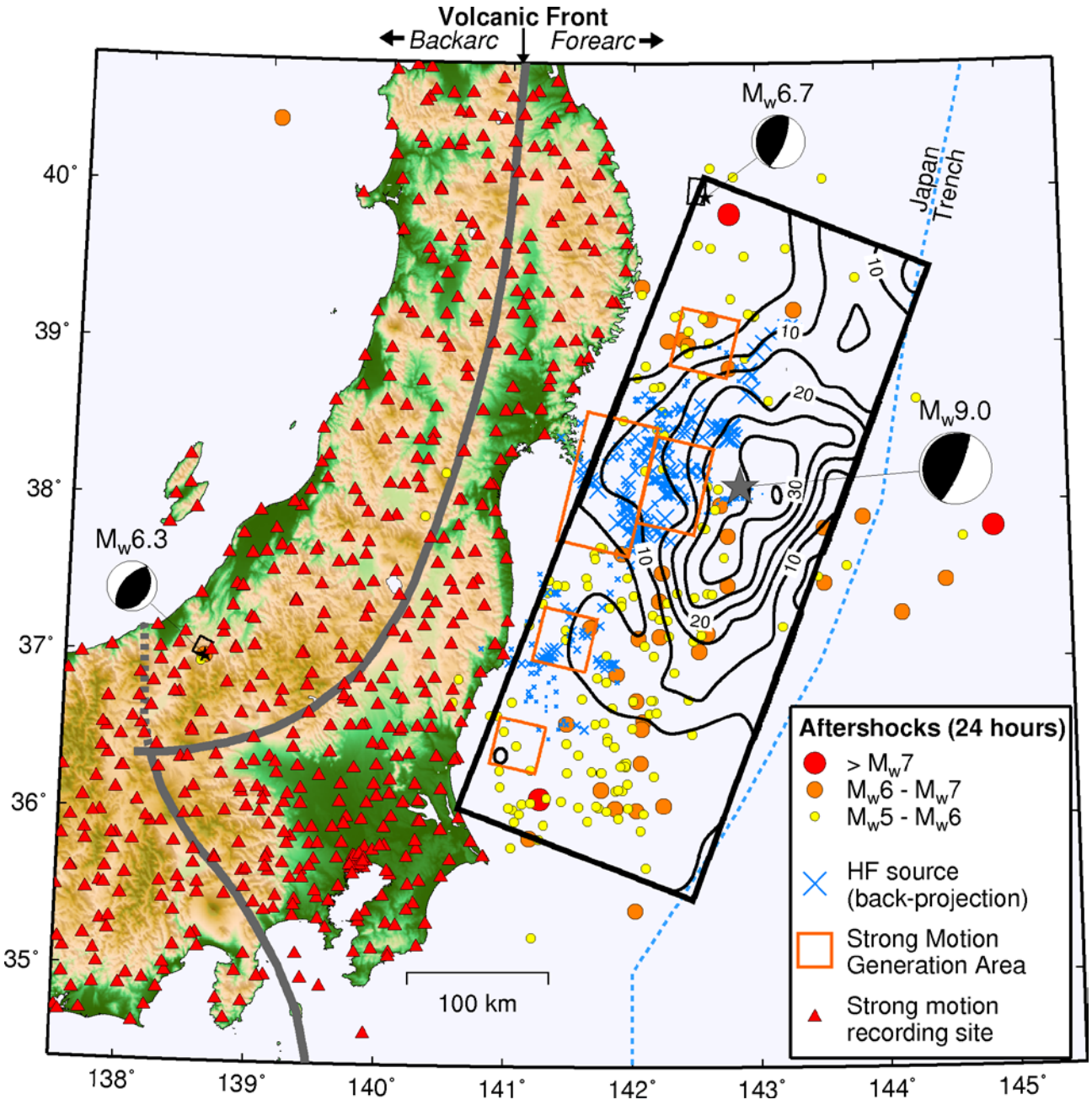

Figure 1. Map view showing surface projections of two selected triggered events for this study (Mw 6.3 crustal event and Mw 6.7 interface event) along with various attributes of mainshock fault model selected by Stewart et al. (2013), which is derived from Yokota et al. (2011). Mainshock fault attributes shown are the Strong Motion Generation Areas of Kurahashi and Irikura (2011) (orange rectangles) and the high-frequency back-projection source locations of Meng et al. (2011) (blue crosses). Contours indicate slip (m) for the Yokota et al. rupture model. Colored circles show aftershocks within the first 24 hours following the mainshock. Dashed blue line indicates location of Japan Trench and the gray star is the JMA epicenter of the mainshock. The red triangles denote the locations of some of the strong motion recording sites considered in our analysis (additional stations were considered beyond the limits of the map).

1. *Location relative to plate boundary.* We sought events on, and inboard from, the plate boundary. This was to see if the forearc/backarc path effects are similar for waves travelling principally in a forearc-to-backarc direction (source to instruments) or vice-versa. We are also interested in event-term trends for these earthquakes relative to the mainshock.
2. *Recordings*. We sought events with numerous uniformly processed recordings using standard Pacific Earthquake Engineering Research (PEER) procedures (Darragh et al., 2004; Chiou et al., 2008) as of 12/2012. The crustal & interface events produced 520 & 472 records.
3. *Magnitude*. We sought events with similar magnitudes.

For the crustal event, we took the fault plane solution of Nagumo (2012). We examined several other fault plane solutions for this event from the JMA web site (http://www.seisvol.kishou.go.jp/eq/sourceprocess/event/201103120359near.pdf, last accessed Dec 2012) and NIED web site (http://cais.gsi.go.jp/YOCHIREN/report/kaihou86/07_04.pdf, last accessed Dec 2012). The Nagumo model was selected because its fault plane solution is most clearly documented. For the interface event, we take the only available fault plane solution, which is from the JMA web site (http://www.seisvol.kishou.go.jp/eq/sourceprocess/ event/20110623near.pdf, last accessed Jan 2013). Both of the selected fault planes are shown in Figure 1.

For both events, we obtained available ground motion records from the Knet and Kik-net arrays at the NIED web site (http://www.kyoshin.bosai.go.jp/kyoshin/, last accessed Dec 2012). A total of 554 and 641 three-component uncorrected digital accelerograms were selected for the crustal and interface events, respectively. Sponsored by the PEER center, those motions were processed by Pacific Engineering and Analysis following PEER/NGA protocols (Darragh et al., 2004; Chiou et al., 2008), which include selection of record-specific corner frequencies to optimize the usable frequency range. For Kik-net sites, only data from the ground surface stations are considered.

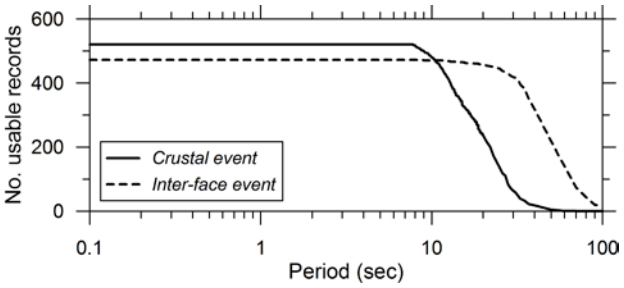

Figure 2. Number of usable two-component horizontal records as function of spectral period for the two data sets

The most important filter is the low-cut filter, which removes low frequency noise effects. We take the minimum usable frequency as $1.25 \times f_{HP}$, where f_{HP} is the high-pass (equivalent to low-cut) corner frequency used in the processing. Using the filtered records, we computed the intensity measures of peak acceleration (PGA), peak velocity (PGV), and pseudo-acceleration response spectra at a range of periods between 0.01 and 10.0 sec. Figure 2 presents the number of usable recordings as a function of period. A usable recording for period T is defined as having both horizontal components with $T < 1/(1.25\ f_{HP})$. The data set is seen to fall off for periods beyond about 10-30 sec.

3. DATA ANALYSIS

3.1 Analysis Procedures

The data analysis follows the same procedures described in Stewart et al. (2013), and hence is described here only briefly. Essentially, we compute total residuals (data minus model in natural log units) using an applicable ground motion prediction equation (GMPE). In this case, we use the Zhao et al. (2006) GMPE. Event terms are computed using the mean of total residuals for conditions where distance attenuation bias is judged to not significantly contaminate the results. Distance attenuation trends are evaluated from the trends of residuals with distance.

A second set of residuals is computed as the difference between data and the GMPE for rock conditions (described in Stewart et al., 2013). These residuals are used to evaluate the scaling of ground motions with the time averaged shear wave velocity in the upper 30 m of the site (V_{s30}).

3.2 Distance Attenuation

Figure 3 shows RotD50 values (i.e, median of single-azimuthal ground motions; Boore, 2010) for PGA, 0.1 s, 1.0 s, and 3.0 s pseudo-acceleration (PSA) at 5% damping versus rupture distance. Also shown in Figure 3a are medians (μ) and medians ± one intra-event standard deviation (ϕ_{ln}) for the ZEA (Zhao et al.) 2006 GMPE for the site category having $V_{s30} \approx 300$ m/s. Figure 4 shows total residuals versus rupture distance. Forearc and backarc sites are distinguished in both Figures 3 and 4.

Several significant trends are evident from Figure 3 and 4. The crustal event occurs in the backarc region and produced backarc recordings from nearly zero distance to large distance. Forearc recordings begin at about 80 km. As shown by the binned median residuals, the forearc recordings have an upward shift relative to the backarc, which is consistent with previously observed trends of faster distance attenuation in backarc than forearc regions (Ghofrani and Atkinson, 2011). This is generally consistent with what we saw with the Tohoku mainshock, but interestingly in this case, the waves are crossing the volcanic front in opposite directions.

The interface event has forearc recordings starting at around 60 km and backarc recordings beginning at about 120 km. Backarc residuals have a clear downward shift relative to the forearc, which is the same trend observed with the Tohoku mainshock data (Ghofrani and Atkinson, 2011; Skarlatoudis and Papazachos, 2012; Stewart et al 2013). Hence, the apparent differences in anelastic attenuation rate in forearc and backarc regions appear to be stable across events and source locations (relative to volcanic front).

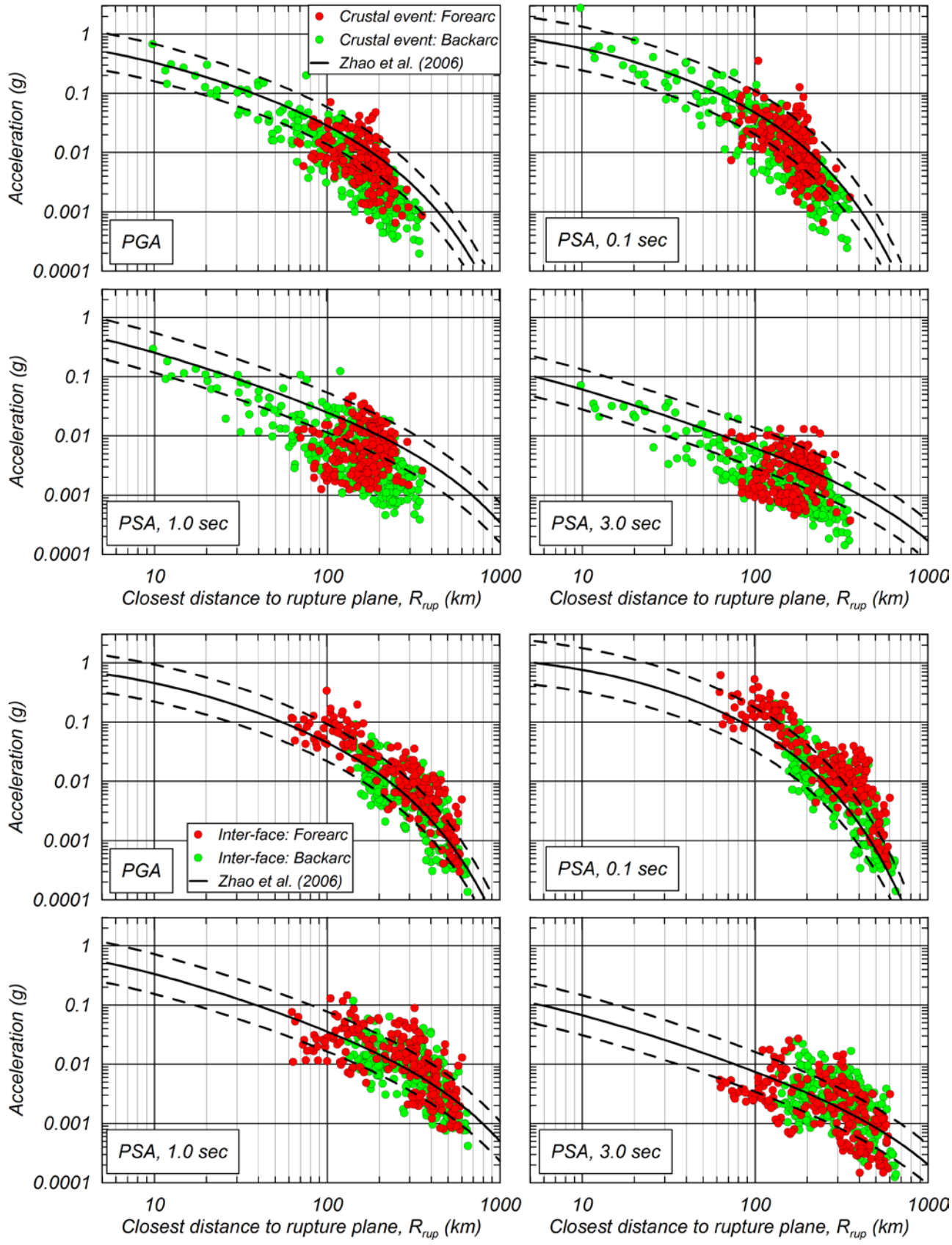

Figure 3. Ground motion intensity measures plotted against distance for crustal (top) and interface (bottom) triggered events. Backarc and forearc records shown with separate symbols. Zhao et al. 2006 GMPE shown for soil site condition.

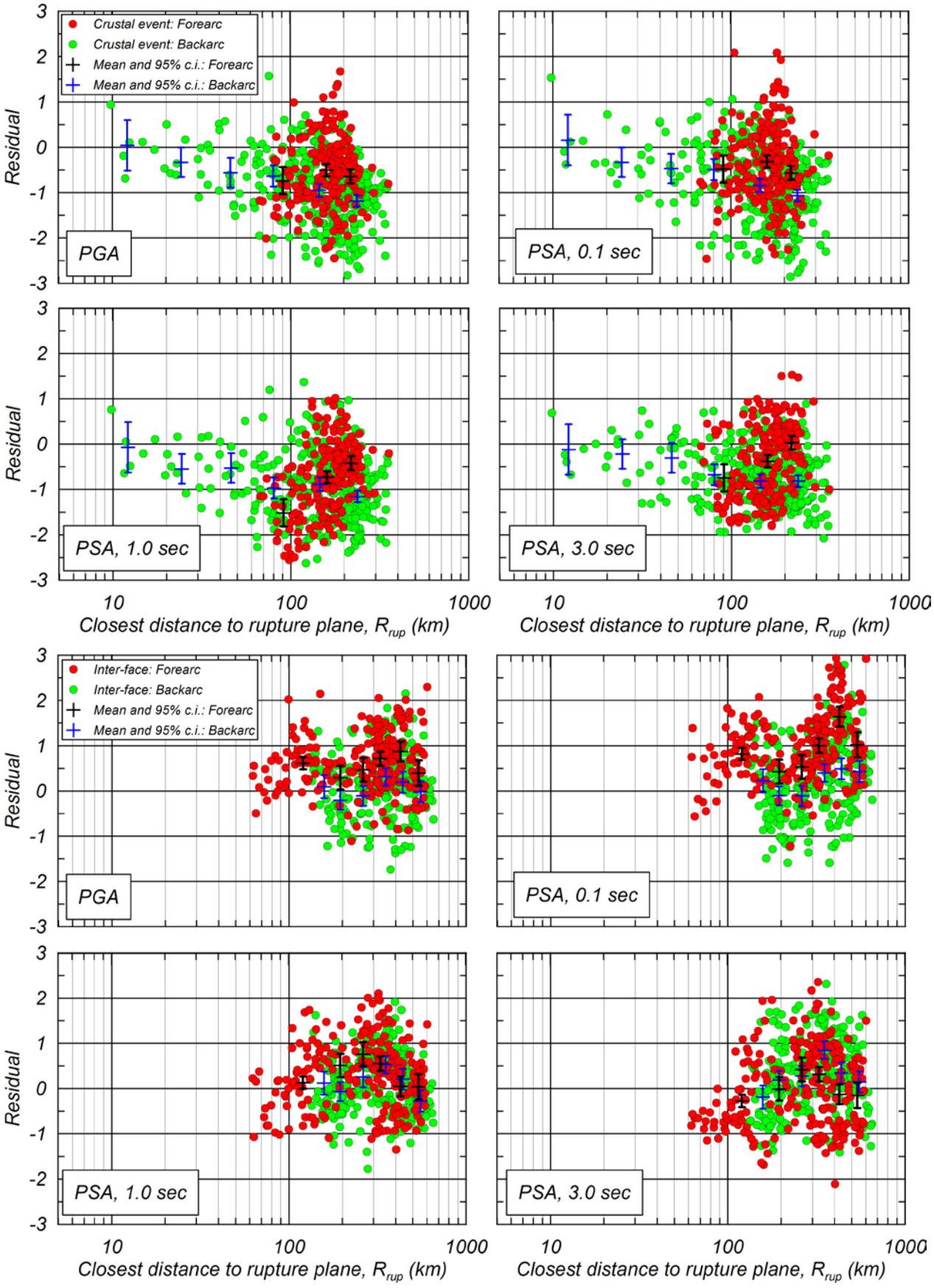

Figure 4. Distance-dependence of total residuals for crustal (top) and interface (bottom) events relative to ZEA 2006 GMPE.

3.3 Event Terms

As shown in Figure 4, in most cases the residuals are not centered at zero ordinate, indicating systematic misfits of the GMPE relative to the data. Since the events are well recorded, this bias is practically equivalent to an event term as would be calculated from a mixed-effects regression (e.g., Abrahamson and Youngs, 1992). Non-zero event terms (η) are typical; what is of interest is to see if the event terms are consistent with event-to-event scatter (represented by event term standard deviation τ) as observed from previous earthquakes. Figure 5 shows event terms, calculated using the following data for the two earthquakes:

1. For the crustal event, we use a combination of backarc recordings with closest distance (R_{rup}) < 70 km and forearc to R_{rup} < 250 km. We include the close-distance backarc records because the distance attenuation is dominated by geometric spreading in that region.
2. For the interface event, we use forearc recordings with R_{rup} < 250 km.

Event terms are taken as median residuals for the ZEA 2006 GMPE as a function of spectral period. Also shown in Figure 5 are the $\pm$ τ model (inter-event standard deviation) from ZEA 2006. We note that the mainshock and interface event terms have a similar trend with period, whereas the crustal event is different because of an increase at long period. One possible explanation for this is stronger surface waves excited by the shallow crustal event compared to the lack of surface waves for the relatively deep interface event. These surface waves would be more pronounced at the longer periods due to the higher attenuation of shorter periods in the shallow crust. Analyses of additional events are needed to determine whether these effects are accidental or systematic.

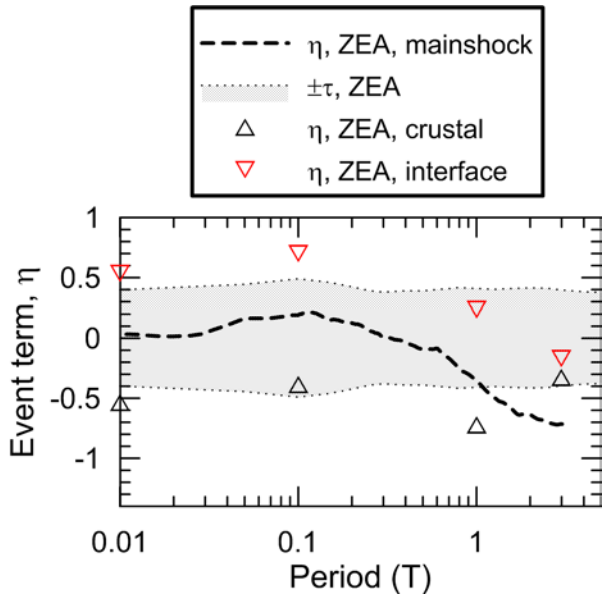

Fig. 5. Estimated event terms of Tohoku-oki mainshock and two triggered events relative to the ZEA 2006 GMPE. Also shown is the ZEA inter-event standard deviation (τ).

3.4 Site Response

A meaningful analysis of site effects from these data sets is complicated by the significant distance attenuation misfits identified in Section 3.2, which cause large non-zero residuals for reasons unrelated to site response. Accordingly, for the analysis of site effects, we use the subset of data used for event term computations (described in Section 3.3), for which distance attenuation trends are relatively well-matched by the ZEA GMPE. We use intra-event reference site residuals, which are total reference site residuals corrected to zero mean through subtraction of the event term (details in Stewart et al. 2013).

Figure 6 shows the trends of ZEA 2006 reference site residuals for the crustal event against V_{s30} for the intensity measures of PGA and PSA at 0.1, 1.0, and 3.0 sec. A log-linear regression is also shown.

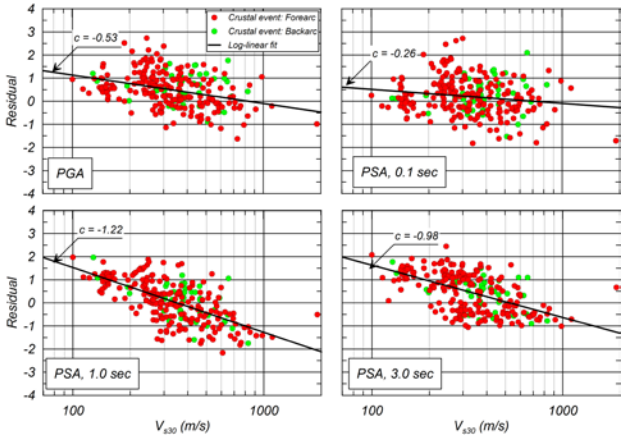

Fig. 6. Reference rock residuals of crustal event using ZEA 2006 GMPE for rock site conditions, showing scaling of site factors with V_{s30}.

Figure 7 shows the slopes of the fit lines (denoted as c) for both events against trends presented previously for the Tohoku mainshock and a representative model for active crustal regions (ACRs; Choi and Stewart, 2005). The slopes from these events differ from those for the mainshock at short periods, having stronger V_{s30} scaling. These differences may be influenced by nonlinearity.

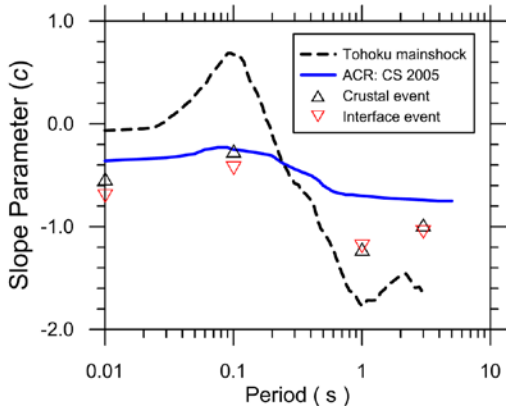

Fig. 7. V_{s30}-scaling of rock residuals (c parameter) from mainshock, subsequent events, and ACR model

4. CONCLUSIONS

In a separate paper investigating the attributes of the Tohoku-oki mainshock data (Stewart et al., 2013), we found important attributes of the ground motions that have substantial practical importance for seismic hazard analysis. Among those attributes were: (*i*) faster anelastic attenuation in the backarc region as compared to the forearc region; (*ii*) positive event terms at short periods that decrease as period increases; and (*iii*) scaling of site amplification with V_{s30} that is substantially reduced from that in active crustal regions at short periods but enhanced at long periods (weaker and stronger V_{s30}-scaling, respectively). We note here that the analysis of site effects from the Tohoku mainshock did not consider nonlinearities.

In this paper, we examine the repeatability of these effects using an admittedly small data set of two events subsequent to the mainshock – one a crustal event in the backarc region and one occurring at the plate interface on the mainshock fault plane. Both events are well recorded and the data was uniformly processed using standard PEER procedures in the same manner as the mainshock data.

We find the variable anelastic attenuation rates to be repeatable, even though one of the considered events occurred on the backarc side of the volcanic front. This is perhaps our most significant finding in this paper. The interface event terms follow a similar form to those from the mainshock, whereas the crustal event shows a different pattern at long periods, but we cannot draw statistically significant inferences from so few earthquakes. The V_{s30}-scaling from these events was much stronger at short periods than had been observed in the mainshock, but relatively consistent at long periods. The differences at short period may be a result of nonlinearity, but further study will be required to understand these differences.

Acknowledgements:

Partial supports for this work to PEER is provided by the USGS/NEHRP and FM Global, and which are gratefully acknowledged.

References:

Abrahamson, NA and RR Youngs (1992). A stable algorithm for regression analyses using the random effects model, *Bull. Seismol. Soc. Am.*, 82, 505–510.

Boore, DM (2010). Orientation-independent, nongeometric-mean measures of seismic intensity from two horizontal components of motion, *Bull. Seismol. Soc. Am.*, 100, 1830 – 1835.

Chiou, B, R Darragh, N Gregor, and WJ Silva (2008), NGA project strong-motion database. *Earthquake Spectra*, 24(1), 23–44.

Choi, Y. and Stewart, J.P. (2005). Nonlinear site amplification as function of 30 m shear wave velocity, *Earthquake Spectra*, 21 (1), 1-30.

Darragh, R, WJ Silva, and N Gregor (2004). Strong motion record processing for the PEER center, Proc. Workshop on Strong Motion Record Processing, Richmond, CA, May 26-27, 2004 (http://www.cosmos-eq.org/recordProcessingPapers.html).

Ghofrani, H and GM Atkinson (2011). Forearc versus backarc attenuation of earthquake ground motion, *Bull. Seismol. Soc. Am.*, 101, 3032–3045.

Kurahashi, S, and K Irikura (2011). Source model for generating strong ground motions during the 2011 off the Pacific coast of Tohoku Earthquake, *Earth Planets Space*, 63, 571-576.

Meng, LS, A Inbal, and JP Ampuero (2011). A window into the complexity of the dynamic rupture of the 2011 Mw 9 Tohoku-Oki earthquake, *Geophys. Res. Lett.*, 38, L00G07, doi:10.1029/2011GL048118.

Nagumo, H. (2012), Rupture process of northern Nagano Prefecture earthquake on March 12th, 2011 (Mj6.7), Annual Meeting of Japan Association for Earthquake Engineering, Japan Association for Earthquake Engineering.

Skarlatoudis, A and CB Papazachos (2012). Preliminary study of the strong ground motions of the Tohoku, Japan, earthquake of 11 March 2011: Assessing the influence of anelastic attenuation and rupture directivity, *Seismol. Research Lett.*, 83, 119-129.

Stewart, JP, S Midorikawa, RW Graves, K Khodaverdi, T Kishida, H Miura, Y Bozorgnia, and KW Campbell (2013). Implications of Mw 9.0 Tohoku-oki Japan earthquake for ground motion scaling with source, path, and site parameters, *Earthquake Spectra*. Accepted.

Yokota, Y, K Koketsu, Y Fujii, K Satake, S Sakai, M Shinohara, and T Kanazawa (2011). Joint inversion of strong motion, teleseismic, geodetic, and tsunami datasets for the rupture process of the 2011 Tohoku earthquake, *Geophys. Res. Lett.* 38, L00G21, doi:10.1029/2011GL050098.

Zhao, JX, J Zhang, A Asano, Y Ohno, T Oouchi, T Takahashi, H Ogawa, K Irikura, HK Thio, PG Somerville, Y Fukushima, and Y Fukushima (2006). Attenuation relations of strong ground motion in Japan using site classification based on predominant period, *Bull. Seismol. Soc. Am.*, 96, 898–913.

3 Site Characteristics of 31 Chilean Seismometer Stations Shaken During the Maule M8.8 Earthquake of 27 February 2010

The February 27, 2010 Maule, Chile earthquake (Mw8.8) is one of the largest earthquakes to occur since 1900. Its effects were felt along over 600 km of the central Chile coast. The event occurred in a subduction zone in which the Nazca plate passes eastward and downward beneath the South American plate. The rate of convergence of the two plates is 70 mm/year. The mainshock occurred at 3:34 am local time on February 27, 2010 with an epicenter located at -36.027°, -72.834° and hypocentral depth of 30 km. Strong shaking lasted for over a minute in some areas, and widespread damage occurred in some cities. A large number of significant aftershocks contributed additional damage to an already fragile infrastructure.

The focus of this task is on the measurement of shear-wave velocity (Vs) of the near-surface materials at strong motion recording stations in Chile. Four data collection campaigns in Chile were carried out by Dr. Robert Kayen of the USGS and his team. Data were collected at 31 stations in the states of Atacama, Coquimbo, Valpariso, Metro Region, Libertador, Maule, Bio Bio, Araucania, and Los Rios. These states are regionally instrumented with permanent seismometer recording stations, though these have been supplemented with more closely spaced temporary aftershock recorders in response to local seismic activity. The Vs profiles are collected and included in the NGA-Sub database to model strong motion site amplifications. Data presented here were gathered using the continuous harmonic sine wave approach for the spectral analysis of surface waves. This method have the advantage for the Chilean sites because many of stations are stiff profiles with weathered bedrock near the surface, by which penetration methods tend not to be useful as they cannot reach the meaningful depths required for seismic site response analysis without expensive drilling. These results are presented in a report entitled: "*Site Amplification Factors for 31 Chilean Seismometer Stations by Spectral Analysis of Surface Wave Dispersion Shaken During the Maule M8.8 Earthquake of 27 February 2010*" by Kayen, R. E., Carkin, B. D., Pinilla, C., Corbet, S., Ng, A., Gorbis, E. and Truong, C.. The report is presented in the following section.

Seismic Velocity Site Characterization of 31 Chilean Seismometer Stations by Spectral Analysis of Surface Wave Dispersion.

By Robert Kayen, Brad D. Carkin, Skye Corbet, Camilo Pinilla, Allan Ng, Edward Gorbis, and Christine Truong

Abstract

We present one-dimensional shear-wave velocity (Vs) profiles at 31 strong motion sites in Chile from Valdivia in southern Chile to Copiapo in the northern Atacama Desert. We estimate the Vs profiles with the spectral analysis of surface waves (SASW) method. The SASW method is a non-invasive method that is useful for indirect estimate of the Vs at depth from variations in the Rayleigh wave phase velocity at the surface. The purpose of the study is to determine the detailed site velocity profile, the average velocity in the upper 30 m of the profile, $V_{s,30}$, the average velocity for the entire profile, $V_{s,Z}$, and the NEHRP site classification.

Introduction

This project focuses on the measurement of shear-wave velocity (V_s) of the near-surface materials at strong motion recording stations in Chile. During four data collection campaigns, data were collected in the states of Atacama, Coquimbo, Valpariso, Metro Region, Libertador, Maule, Bio Bio, Araucania, and Los Rios. These states are regionally instrumented with permanent seismometer recording stations, though these have been supplemented with more closely spaced temporary aftershock recorders in response to local seismic activity. The V_s profiles presented in this report are collected for calibration of strong motion site amplification models based on direct measurement of velocity, by topography, or by surface geologic unit. Data presented here were gathered using the continuous harmonic sine wave approach for the spectral analysis of surface waves presented by Kayen et al. (2004, 2013), which is a stepped-sine wave method that utilizes a notch-filter methodology that improves on the approach of Satoh et al. (1991). CSS-SASW is an inexpensive and efficient means of non-invasively estimating the near-surface V_s of the ground. Though it is possible to measure V_s in cased boreholes or during penetration tests these approaches tend not to be useful for evaluation of Chilean strong motion sites as they cannot reach the meaningful depths required for seismic site response analysis without expensive drilling and casing. Because many of the Chilean sites are stiff profiles with weathered bedrock near the surface penetration methods are not useful.

Maule Earthquake

The February 27, 2010 Maule, Chile earthquake (Mw = 8.8) is the fifth largest earthquake to occur since 1900. Its effects were felt along over 600 km of the central Chile coast. The Mw = 8.8 Offshore Maule, Chile earthquake occurred in a subduction zone in which the Nazca plate passes eastward and downward beneath the South American plate. The rate of convergence of the two plates is 70 mm/year. The mainshock occurred at 3:34 am local time on February 27, 2010 with an epicenter located at -36.027°, -72.834° and hypocentral depth of 30 km. Field observations suggest that tectonic displacement of the hanging wall produced both uplift of over 2 m and subsidence of up to 1 m in coastal regions. Strong shaking lasted for over a minute in some areas, and widespread damage occurred in some cities. A large number of significant aftershocks contributed additional damage to an already fragile infrastructure.

Study Sites

Between September 25, 2012 and June 25, 2013 testing was performed at 31 sites across a broad region of Chile from Latitude 40°S in Valdivia, Region de Los Rios to Latitude 27°S in Copiapo, Atacama Region.. The V_S profiles presented in this report are for local site conditions in nine Administrative regions in Chile and are reported in Table 1.

Figure 1. Surface wave test locations for 31 sites in Chile affected by the 2010 Maule M8.8 earthquake.

ID	Station	SASW Test #	Vs30 Man.	Vs30 Auto.	NEHRP Man.	NEHRP Auto.	PGA (g) 2/27/10	Latitude	Longitude	Site
1	COPI	993COPI	349	339	D	D	0.022	-27.374	-70.322	COPIAP-HOSPITAL
2	VALLE	992VALLE	561	549	C	C	0.019	-28.576	-70.755	VALLENAR-HOSPITAL
3	PAP	991PAPU	687	714	C	C	0.352	-32.507	-71.448	PAPUDO
4	ROBL	990ROBLE	1951	1999	A	A	0.188	-32.976	-71.016	CERRO EL ROBLE
5	OLMU	981-OLMU	372	376	C	C	0.354	-32.994	-71.173	OLMU-Casa
6	VINA	979VIN	289	290	D	D	0.27	-33.0253	-71.553	VINA DEL MAR
7	VALU	967VALU	925.6	1026	B	B	0.204	-33.035	-71.596	VALPARASO-UTFSM
8	MAR	980MAR	280	261	D	D	0.345	-33.048	-71.51	VDM-MARGA MARGA
9	VAL	968VALP	454	429	C	C	0.244	-33.048	-71.604	VALPARASO-Almendral
10	CASB	983CASB	303	312	D	D	0.328	-33.321	-71.411	CASABLANCA-Teatro
11	LCON	963LCON	619	615	C	C	0.224	-33.396	-70.537	LASCONDES
12	SLUC	965SLUC	1411	1400	B	B	0.338	-33.441	-70.643	SANTIAGO-CerroSTA. LUCIA
13	LRNA	964LRN	574	615	C	C	0.308	-33.452	-70.531	LA REINA
14	SANT	966SANT	420	483	C	C	0.26	-33.467	-70.652	SANTIAGO-Conjunto
15	HTIS	962HTIS	383	409	C	C	0.294	-33.501	-70.579	PENALOLEN-Hospital
16	CRMA	985CRMA	428	466	C	C	0.518	-33.509	-70.772	MAIP-Centro
17	MET	988MET	598	638	C	C	0.197	-33.514	-70.606	LA FLORIDA METRO
18	ANTU	970ANTU	621	621	C	C	0.272	-33.569	-70.634	LA PINTANA
19	HSOR	989HSOR	867	815	B	B	0.264	-33.577	-70.581	PUENTEALTO HOSP
20	LLO	984LLO	308	314	D	D	0.424	-33.616	-71.611	LLOLLEO
21	SNJM	969SJM	495	491	C	C	0.48	-33.641	-70.354	SAN JOSE DE MAIPO
22	MELP	986MELP	636	620	C	C	0.777	-33.687	-71.214	MELIPILLA-Compaa
23	MAT	987MAT	370	372	C	C	0.325	-33.96	-71.873	MATANZAS-Escuela
24	HUAL	973HUA	528	541	C	C	0.423	-34.977	-71.805	HUALA-Hospital
25	CURI	971CUR	537	510	C	C	0.439	-34.99	-71.236	CURIC-Hospital
26	CONT	974CONST	274	NO SOL	D		0.594	-35.34	-72.406	CONSTITUCIN-Hospital
27	TAL	972TAL	548	551	C	C	0.45	-35.43	-71.665	TALCA-Colegio Integrado SAN PO X
28	CONC	977CONC	349	363	D	C	0.338	-36.828	-73.048	CONCEPCIN-Colegio Inmaculada Concepcin
29	CCSP	978CCSP	332	340	D	D	0.649	-36.844	-73.109	CONCEPCIN-Colegio San Pedro De La Paz
30	ANGO	975ANG	417	419	C	C	0.796	-37.795	-72.706	ANGOL-Hospital
31	VALD	976VLD	454	429	C	C	0.113	-39.831	-73.239	QDR

Table 1. Chilean seismometer, SASW test number, inversion Vs30's, NEHRP code, PGA from Maule event, latitude, longitude, site name.

REGION A: SANTIAGO AREA

Stations near the city of Santiago experienced an average peak ground acceleration is about 0.32g. Fig. 2 shows that 9 stations are located within a circle of 15 km radius. One station San Jose De Maipo (SNJM) is located on a thick fluvial gravel deposit in a river valley above and south of the city of Santiago. All stations are located on the gravel soils and that shear wave velocities were available for three stations by two different survey methods.

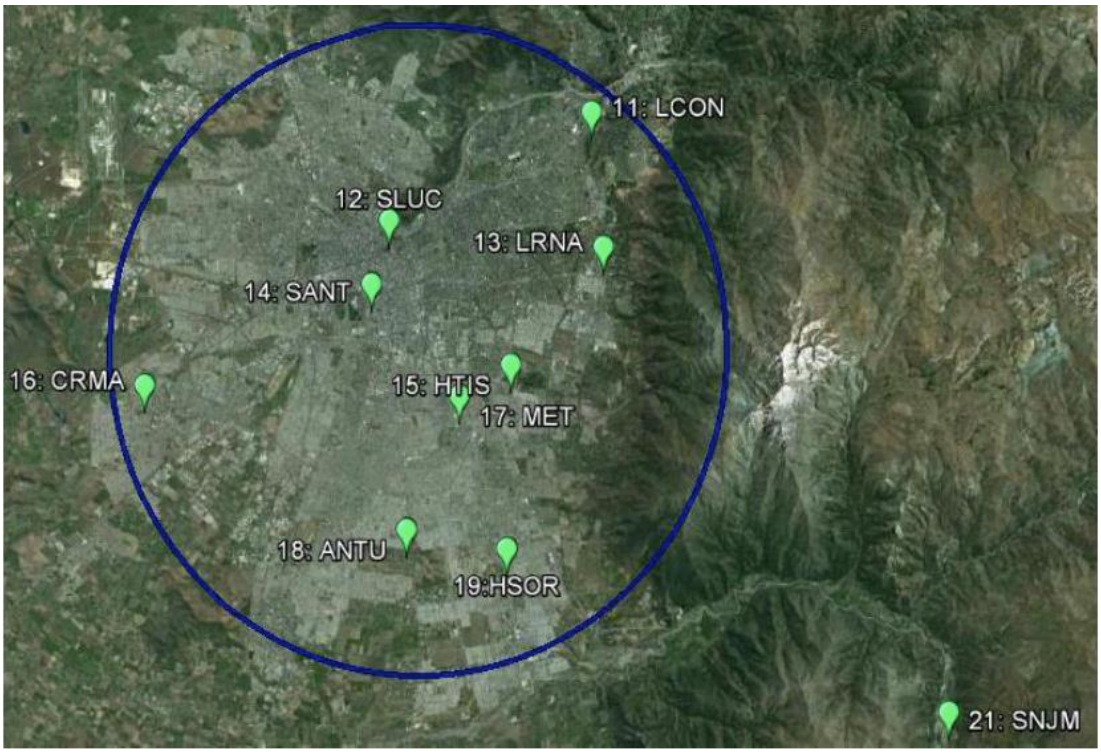

Figure 2. Station Locations in the Santiago, Metropolitan Region and Libertador Region.

REGION B: VALPARAISO AREA

Four stations are located in Valparaiso and Vin del Mar where an average peak ground acceleration of 0.32g was felt. Fig. 3 shows that there are four stations in this area within a 10 km area. This region was studied by Midorikawa (1991) by comparing the acceleration recordings at rock site (VALU) and soil sites (VINA and VAL). That report describes a Vs profile estimated at VINA from the boring, and measured at Station VAL (Vs profile available by Sargoni 2005). The paper by Midorikawa also mentioned that VINA may have soil-structure interaction effect due to the adjacent building. The paper describes granite rock exposed at Station VALU for which V_{s30} was estimated as 1300 m/s by Arenda and Saragoni (1994), and Saragoni (2005). V_{s30} at Station MAR is estimated at 280 m/s by Daza (2003).

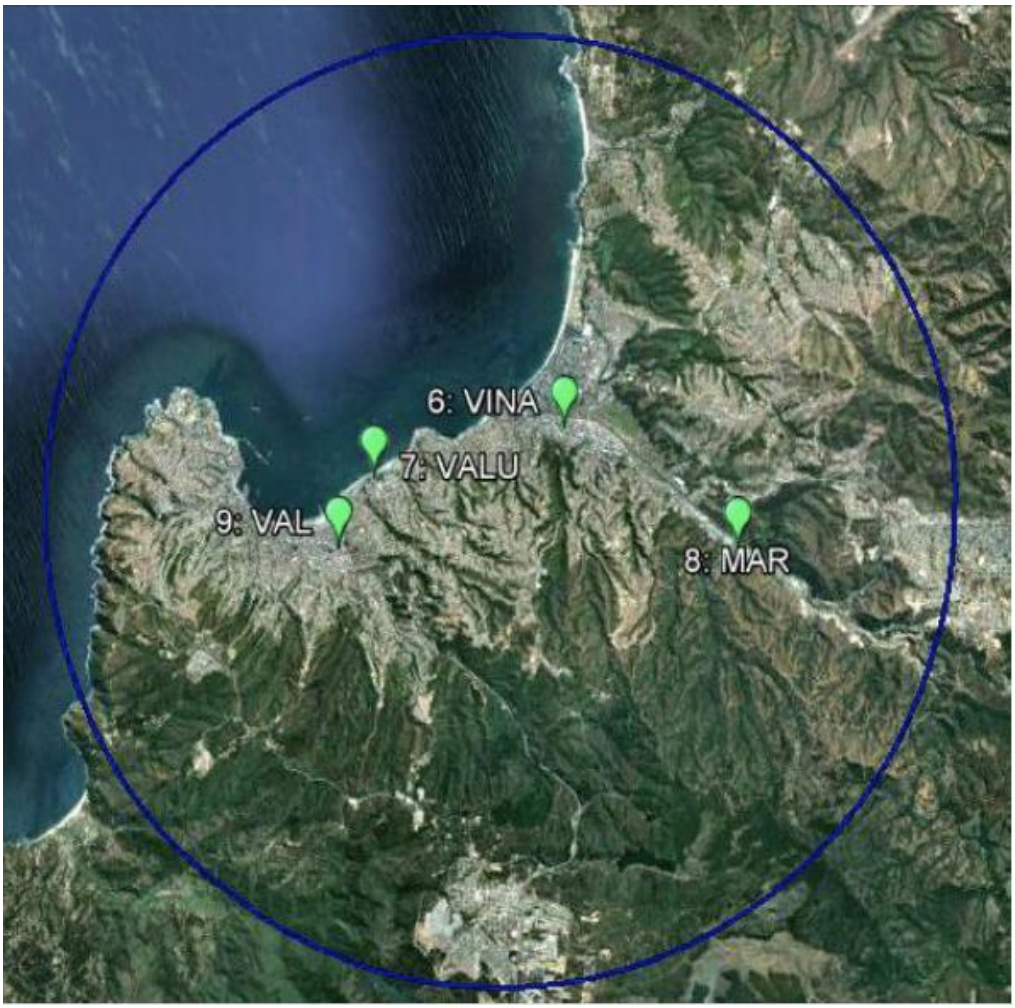

Figure 3. Station Locations at Valparaiso, and Vin Del Mar, Valpariso Region

REGION C: SAN ANTONIO AREA

Four stations near the city of San Antonio felt an average peak ground acceleration of 0.46g. Fig. 4 shows that the four stations within a circle of 40 km radius that means that CASB is about 80 km away from MAT. Of the four stations, down-hole measurements are available at CASB, MELP, and MAT by Boroscheck et al. (2012). The other station (LLO) also has a Vs30 profile up to 19 m (Arenda and Saragoni, 1994).

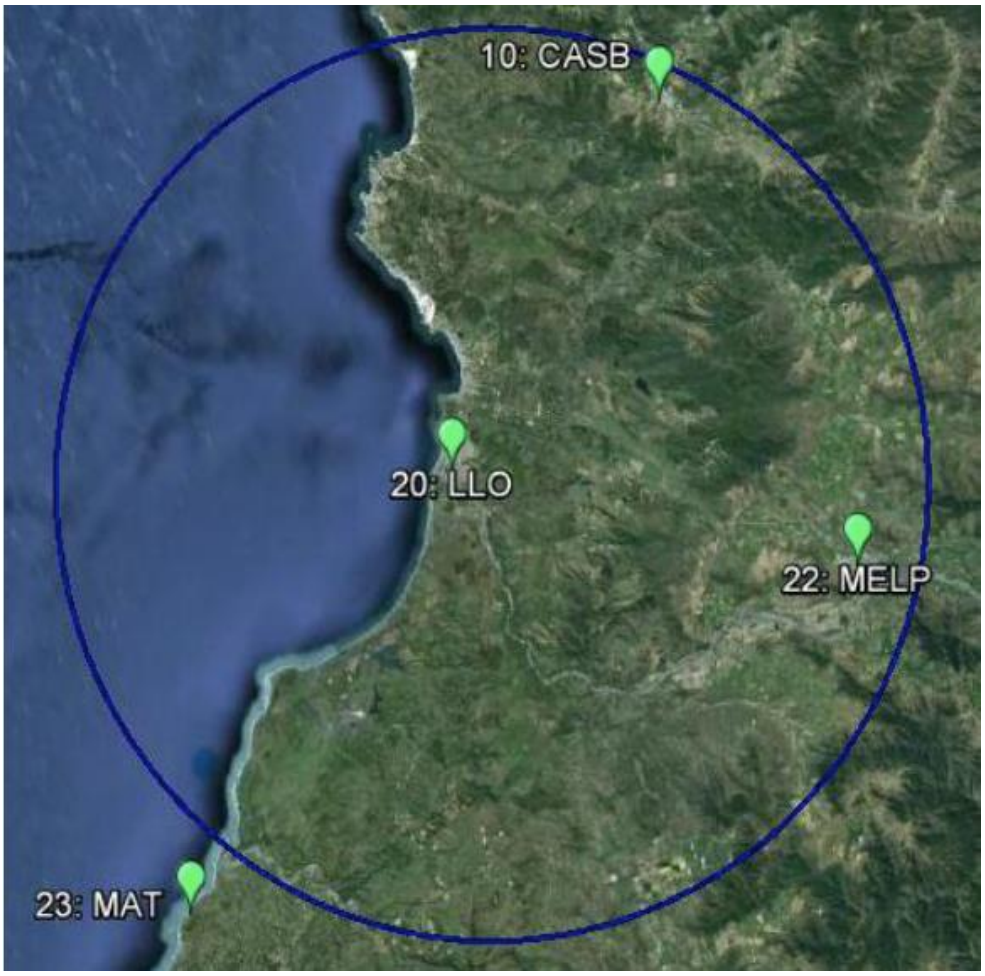

Figure 4. Station Locations in the San Antonio Region

REGION D: TALCA AREA

Four stations near city of Talca felt an average peak ground accelerations is 0.48g. Fig. 4 shows these within a circle of 40 km radius that means that CURI is about 110 km away from CONT. Shear wave velocity measurements are available for all these stations by down-hole method (Boroscheck et al. 2012) and micro-tremor measurements (Kataoka 2011).

Figure 5. Station locations in the Maule region near Talca. Constitucion, Curico, and Hualane.

REGIONS E & F: OLMUE AREA AND PAPUDO

Three stations are near the City of Olmue and Papudo and felt an average peak ground accelerations is 0.27g in Olmue area and 0.45g in Papudo. Fig. 6 shows that there are two stations within a circle of 10 km radius at city of Olmue and one station in city of Papudo, those are separated by 60 km. There is no available shear wave velocity measurement for two stations (ROBL, OLMU) in Olmue. In City of Papudo, the shear wave velocity profile is available up to depth of 16 m (Arenda and Saragoni 1994).

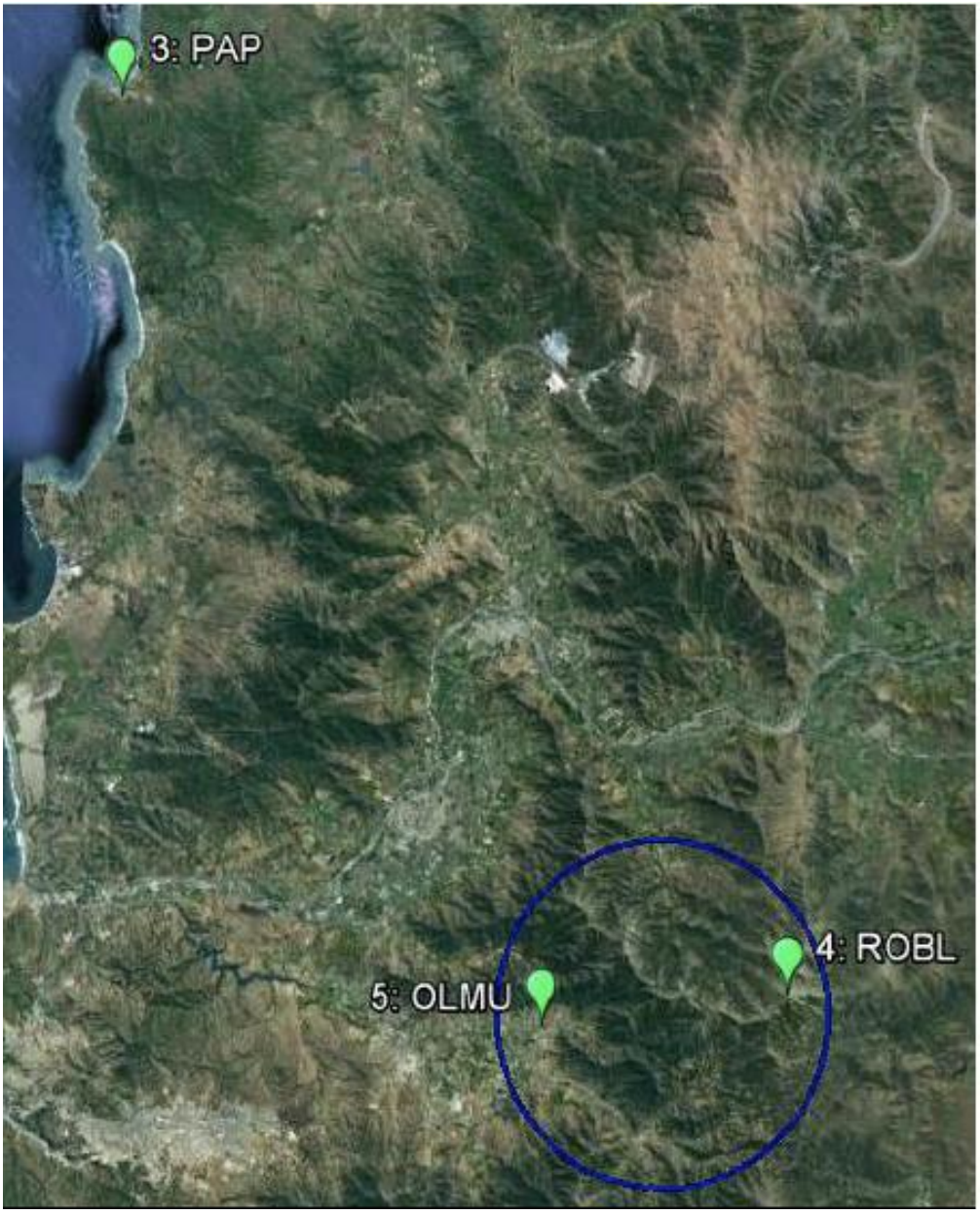

Figure 6. Station Locations near Olmue and Papudon northwest of Santiago.

REGION G: CONCEPCION AREA

Two station are located near City of Concepcion and these felt an average peak ground accelerations is 0.49g. Fig. 7 shows the two stations within a circle of 5 km radius. Both stations have shear wave velocity measurements by Boroscheck et al. (2012) and Unviersity of Chile (2012).

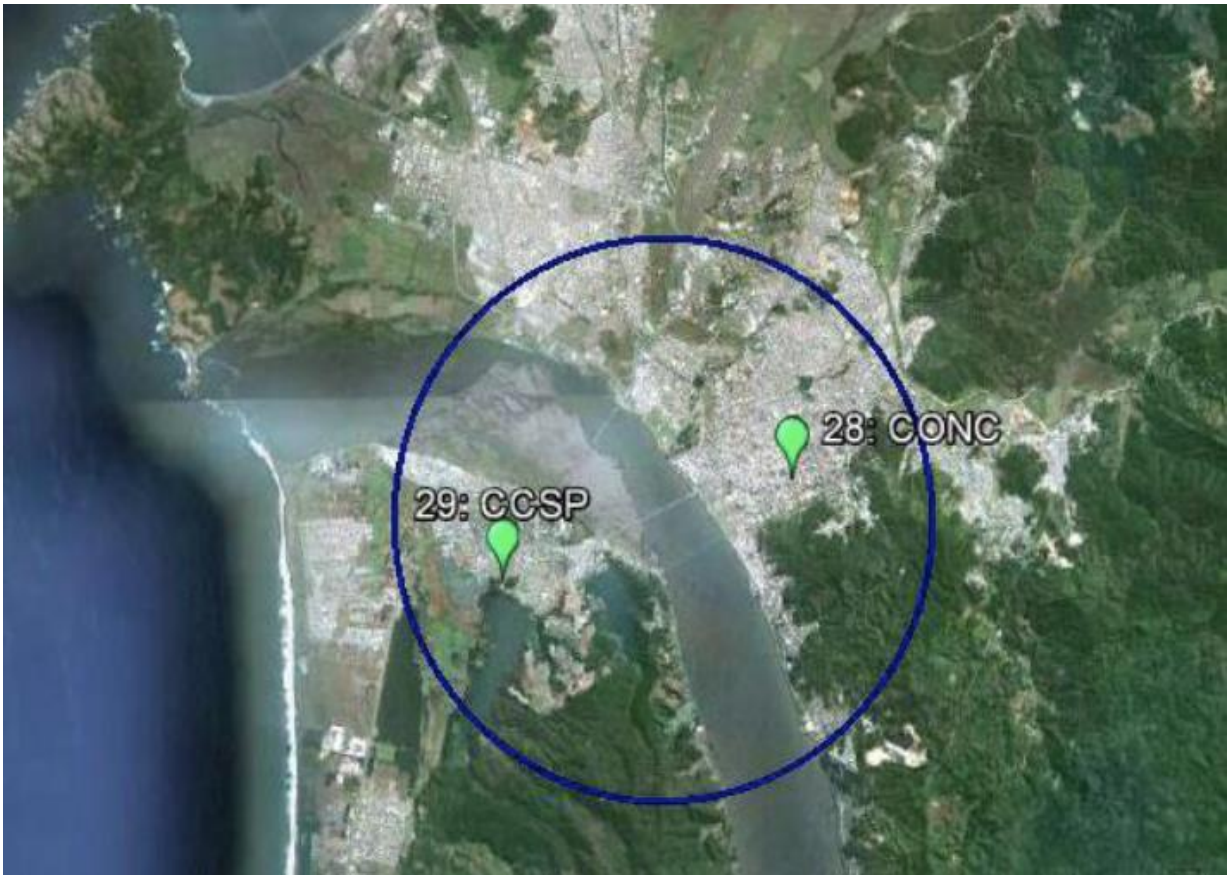

Figure 7 Station Locations near Concepcion City, Bio Bio.

REGIONS H & I: ANGOL AND VALDIVIA AREAS

One station, each, is located in the City of Angol and City of Valdivia. Peak ground accelerations of 0.80g in Angol and 0.11g in Valdivia, respectively were felt during the Maule earthquake. Fig. 8 shows that two stations separated by 240 km. Shear wave velocity is available at ANGO in Angol (Boroscheck et al. 2012), but not available at VALD in Valdivia.

Figure 8 Station Locations near Angol and Valdiva Areas, Region De Los Rios.

REGION J: COPIAPO AREA

Fig. 9 show the station information and these locations near city of Copiapo. Peak ground accelerations were 0.022g at COPI and 0.019g at VALL, respectively. Fig. 9 shows that two stations are separated by 140 km, and VALL is about 500 km north to city of Santiago. Since the shaking level is small and far away from the other stations, these sites are low priority to obtain shear wave velocity profiles.

Figure 9 Station Locations near Vallenar, Coquimbo and Copiapo, Atacama

Rayleigh Wave Dispersion

Active-source surface wave analysis testing typically profiles the upper tens of meters of the ground using drop weights or harmonic sources. The upper 30 m is needed to compute the widely used site parameter V_{S30}, defined as 30 m divided by the shear-wave travel time to 30 m depth. The SASW method employed in this study by the USGS is a technique that uses a parallel array of mass shakers. This method allows for profiling to depths up to 100 hundred meters without the use of massive drop weights or heavy track-mounted machinery. For this method, we substitute an array of many low frequency, 100Hz-1Hz range, electro-mechanical shakers. Surface waves are generated with an array of up to several APS Dynamics Model 400 shakers and amplifier units, powered by a generator and controlled by a spectral analyzer/

The shakers have a long-stroke capable of cycling to as low as 1 Hz. The output signal from the spectral analyzer is split into a parallel circuit and sent to the separate amplifiers. The amplifiers power the shakers to produce a continuously vibrating, coherent, in-phase harmonic-wave that vertically loads the ground. Most of this energy produces Rayleigh retrograde elliptical surface waves that propagate away from the source in a vertical cylindrical wavefront perpendicular to the ground surface. The amplitude of the surface waves decay exponentially with depth, such that the energy of the wavefront is centered at a depth of approximately 1/3 to 1/2 the wavelength.

Frequency domain analyses are made on two or more signals received by sensors placed in the field in the linear array some distance from the source. First, all channels of time domain data are transformed into their equivalent linear spectrum in the frequency domain using a Fourier transform. One of the sensor's signals (typically the sensor closest to the source) is used for a reference input signal, and the other sensor signals are used to compute the linear spectrums of the output. The separation of the reference seismometer and output seismometer ($d_s - d_{ref}$) radially from the source is later used to compute the wave velocity. The cross power spectrum $G_{xy}(\omega)$ is determined by multiplying the complex conjugate of the linear spectrum of the input signal $S_x^*(\omega)$, and the real portion of the linear spectrum of the output signal $S_y(\omega)$. The cross power spectrum is defined as

$$G_{xy}(\omega) = S_x^*(\omega) * S_y(\omega) \quad (1)$$

The autopower spectrum, a measure of the energy at each frequency of the sweep, can be used to determine the strength of individual frequencies, and is equal to the linear spectrum of a given sensor times its complex conjugate pair:

$$G_{xx}(\omega) = S_x(\omega) * S_x^*(\omega), \text{ and} \quad (2)$$

$$G_{yy}(\omega) = S_y(\omega) * S_y^*(\omega). \quad (3)$$

A cross power spectrum can be represented by its real and imaginary components for by its phase θ, and magnitude m. The phase θ is the relative lag between the signals at each frequency, and the magnitude is a measure of the power between the two signals at each frequency. Because the phases are relative they can be stacked to enhance signal-to-noise ratio of the phase lag at each frequency.

The phase of the cross power spectrum is computed as the inverse tangent of the ratio of the imaginary and real portions of the cross power spectrum:

$$\theta_{xy}(\omega) = tan^{-1} \frac{Im(G_{xy}(\omega))}{Re(G_{xy}(\omega))} \quad (4)$$

The travel time t(f) of one cycle of a wave of frequency (f) is computed as,

$$t(f) = \theta(\omega)/\omega \quad (5)$$

and the wavelength, λ, at each frequency is

$$\lambda(\theta) = (d_s - d_{ref})/ \theta(f) \quad (6)$$

The Rayleigh wave velocity, V_r , is computed as

$$\begin{aligned} V_r(f) &= (d_s - d_{ref})/t(f) \quad (7) \\ &= f \bullet (d_s - d_{ref})\ 360°/\theta \ \text{(degrees)} \\ &= f \bullet (d_s - d_{ref})\ 2\pi/\theta(\phi) \ \text{(radians)} \\ &= f \bullet \lambda(f) \end{aligned}$$

The SASW procedure maps the change in θ across the frequency spectrum, and merges these phase lags with the sensor array geometry to measure velocity. Typically with the shaker source the discrete frequencies are cycled in a swept (stepped)-sine fashion across a range of low frequencies (1-200 Hz). Rayleigh-wave phase velocity is then mapped in frequency or wavelength space. This velocity map or profile is called a dispersion curve and characterizes changes in the frequency-dependent Rayleigh wave velocity. The evaluation of velocities is constrained to the wavelength zone where $\lambda(f)/3 < (d_s - d_{ref}) < 2\,\lambda(f)$ for typical data and $\lambda(f)/3 < (d_s - d_{ref}) < 3\,\lambda(f)$ for excellent data, corresponding to phase lags of 180°-1080° (typical data) and 120°-1080° (excellent data). At longer and shorter wavelengths the data become unreliable for computing velocities.

As the useable wavelengths are constrained by the seismometer separation, the array is expanded to capture Rayleigh wave dispersion representative of a specific range of wavelengths. The near surface is characterized by short wavelengths and high frequencies, whereas the deeper portion of the profile is characterized by long wavelengths and low frequencies. Each wavelength range requires a separate independent test that is merged together with other wavelength ranges to determine an average dispersion curve for the site.

At the largest seismometer separations, the increasing area of the wave front causes the wave amplitude to diminish due to geometric damping, and the overall quality of the data diminishes. Two measures of data quality are used to evaluate the field measurements in the frequency domain. Coherence, $\gamma^2(\omega)$, is a normalized real function with values between 0 and 1 corresponding to the ratio of the power of the cross power spectrum, $G_{yx}(\omega) \bullet G_{yx}^{*}(\omega)$, to the autopower spectrum of the outboard seismometer, $G_{xx}(\omega) \bullet G_{yy}(\omega)$. Values close to 1 indicate high correlation between the reference and outboard seismometers across narrow frequency bands. This is a useful data quality parameter for hammer impact data.

$$\gamma_{xy}^2(\omega) = \frac{G_{yx}(\omega) \bullet G_{yx}^*(\omega)}{G_{xx}(\omega) \bullet G_{yy}(\omega)} \quad (8)$$

For swept sine data where discrete frequencies are used to compute phase rather than narrow frequency bands, the frequency response function, FRF, is a complex measure of the data quality of the output (outboard) seismometer, and is sometimes called the Transfer Function:

$$\mathrm{FRF}(\omega) = \frac{G_{yx}(\omega)}{G_{xx}(\omega)} \quad (9)$$

where x is the input (reference) signal and y is the response (output) signal.
The Frequency Response Function is a two-sided complex parameter. To convert to the frequency response gain (magnitude) that is used to evaluate the amplitude of the output response to the input stimulus, a rectangular-to-polar coordinate conversion is used.

Adjustments for missing 1st Wrapped Phase

At some sensor separations the field data have a poorly formed 1st phase such that the first clear wrapped phase crossing occurs not at 180°, but at 540°. For these dispersion data files, a simple reprocessing was done to add one phase jump (360°, 2π) to the dispersion curves preceding the 540° jump to adjust the file to the correct wrapped phase number. This adjustment corrects the wavelength calculation as follows:

$$\lambda_{(\text{corrected})} = 2\pi d/(\theta + 2\pi) \quad (10)$$

With the wavelength adjusted, the velocity, V_R, decreases by

$$V_r = f \bullet 2\pi d/(\theta + 2\pi) \quad (11)$$

The effect of correcting the phase wrap and reducing the calculated wavelength is to reduce the depth of influence of the adjusted dispersion curve.

Inversion of the V_s Profile

The relation between Rayleigh wave (V_R), shear wave (V_S) and compression wave (V_P) velocities can be formulated through Navier's equations for dynamic equilibrium. On the surface of the ground, and in the case of plane strain, the following characteristic equation.

$$\frac{V_r^6}{V_s} - 8\frac{V_r^4}{V_s} + \left(24 - 16\left[\frac{1-2\nu}{2(1-\nu)}\right]\right)\frac{V_r^2}{V_s} + 16\left[\left[\frac{1-2\nu}{2(1-\nu)}\right] - 1\right] = 0 \quad (12)$$

where ν is the Poisson ratio and

$$\frac{V_S}{V_P} = \gamma = \sqrt{\left[\frac{1-2\nu}{2(1-\nu)}\right]} \quad (13)$$

For reasonable values of Poisson Ratio for earth materials, between 0.20 and 0.49, Viktorov (1967) shows that the shear wave velocity ranges between 105%-115% of the measured Rayleigh wave velocity.

$$\frac{V_R}{V_S} = K = \frac{0.87+1.12\nu}{1+\nu} \tag{14}$$

such that across the range $0.2<\nu<0.49$, the range of K is $0.87<K<0.96$.

The inversion method seeks to infer an acceptable best-fit *model* of seismic shear wave velocity, V_S, of the ground given the *measured* dispersive characteristics of Rayleigh waves observed in the frequency domian, and the estimated profile of Poisson ratio and material density. The inversion attempts to build a model from observations, as opposed to the normal prediction of behavior based upon a model. If the inversion model is simple and linear, it will result in a unique and stable solution. The French mathematician Hadamard defined mathematical problems that have solutions that exist, are unique, and are stable as "well-posed" (Zhdanov, 2002). On the other hand, surface wave inversion is an "ill-posed" inverse problem, as solutions are not unique, the solutions may become unstable, and multiple shear way velocity profiles can result in approximately the same dispersion curve (Zhdanov, 2002).

The dispersive characteristic of Rayleigh wave propagation allows us to infer the V_S at depth based on measurements at the free surface. The inversion problem computes the Rayleigh wave phase velocity (V_R) from laterally constant layers of an infinite half space. For each of these layers the shear modulus, Poisson ratio, density, and thickness are unknown. Displacements for a vertically acting harmonic point load can be computed as follows in the far field if we neglect body wave components:

$$u_\beta(r,z,\omega) = F_z \cdot G_\beta \cdot (r,z,\omega) \cdot e^{i[\omega t - \psi_\beta(r,z,\omega)]} \tag{15}$$

where β stands for the generic component either vertical or radial, $G_\beta(\rho,\zeta,\omega)$ is the Rayleigh geometrical spreading function, and $\Psi_\beta(\rho,\zeta,\omega)$ is the composite phase function (Lai, 1998)

Regularization methods have been developed for solving the ill-posed inversion problem: for example the velocity profiles computed here. The Levenberg-Marquardt method, also called damped least squares, is one example of a regularization method. These and other techniques, such as artificial neural networks and genetic algorithms, are discussed by Santamarina and Fratta (1998). One cost of these stochastic methods is that they often require many more iterations, and so they are much more computationally intensive.

The parameters of the inversion problem can be chosen such that the difference between the observational dispersion data and the output of the inversionproblem are minimized. Such a constraint is insufficient for ill-posed problems because many solutions can fit the data equally well and some of these solutions will be physically unrealistic. The most common approach is to constrain the inversion solution space by selecting the smoothest solution from a suite of solutions

that all exhibit a sufficient goodness-of-fit to the observed data, as indicated by a root mean square (RMS) error minimum

An empirical approach serves as a counterpoint to the inversion methods used in this report. Pelekis and Athanosopoulos (2011) advanced the work of Satoh et al. (1991) in a technique termed the (Simplified Inversion Method) SIM method that computes the shear wave velocity profile as a function of the incremental slope of the Rayleigh wave dispersion curve where:

$$V_{Sn,normal\ dispersion} = 1.1 \cdot \frac{\bar{V}_{Rn}D_n - \bar{V}_{Rn-1}D_{n-1}}{D_n - D_{n-1}} \quad (16)$$

$$V_{Sn,inverted\ dispersion} = 1.1 \cdot \frac{D_n - D_{n-1}}{D_n/\bar{V}_{Rn} - D_{n-1}/\bar{V}_{Rn-1}} \quad (17)$$

The dispersion curve V_R plotted against λ_R is converted into an apparent velocity ($\bar{V}_R$) and depth (z) by converting λ_R to an estimated depth of $z_{eq} = a_R \cdot \lambda_R \approx 0.635\lambda_R$. The parameter a_R is a penetration depth coefficient optimized to achieve a minimum weighted average difference between the simplified velocity profile and that computed through the more advanced inversion of Pelekis and Athansopoulos (2011) . The apparent phase velocity, $\overline{V_R}$ is approximated as the velocity at each segment node (layer interface) of a multi-linear curve fit to the dispersion curve. A positive slope of a segment indicates normal dispersion, a negative slope indicates inverted dispersion. The value of V_S for each individual layer is calculated using the equations above for the cases of normal dispersion or inverted dispersion, respectively. The approach of Pelekis and Athansopoulos (2011) improves on the Satoh and others (1991) method notably by optimizing the penetration depth coefficient a_R.

Results

We provide two profile solutions at each site (Inversion and SIM model). We varied the assumptions about the layer thicknesses and the threshold RMS error that determines if the inversion has converged to best characterize the site. The decision as to whether or not the more complex model is warranted by the fit of the theoretical dispersion curve (TDC) to the empirical dispersion curve (EDC) is subjective. Table 1 summarizes results and provides the SASW site ID, the site description, the date of data collection, the latitude and longitude of the SASW test site and the V_{S30}.

Appendix A includes plots of the model profiles and the EDC and TDC's for each site. Appendix A also includes the site photos and a vicinity map for each site. Where possible we have indicated the location of the strong motion station in the site photographs and vicinity maps to assess the distance between the SASW survey and the strong motion station. NEHRP classification is used to average the site conditions in the upper-30 meters of ground (V_{s30} from the IBC, 2002). Equation 18 is used to compute this average velocity based on the unit layer thickness (d_i) and the corresponding interval-velocity (V_{Si}).

$$V_{\substack{S-depth-\\averaged}} = \frac{\sum_{i=1}^{n} d_i}{\sum_{i=1}^{n} \frac{d_i}{V_{Si}}} \qquad (18)$$

These site categories are used to assign design spectra in the evaluation of performance for new and built structures

References Cited

Constable, S.C., Parker, R.L., and Constable, G.G. (1987) Occam's Inversion: A Practical Algorithm for Generating Smooth Models from Electromagnetic Sounding Data. *Geophysics*, 52, 289-300.

Hisada, Y., (1994) An Efficient Method for Computing Green's Functions for a Layered Half-Space with Sources and Receivers at Close Depths, *Bull. Seism. Soc. Am.*, 84, 1456-1472.

Kayen R., Seed R. B., Moss R. E.S., Cetin K. O., Tanaka Y., and Tokimatsu K. (2004) Global shear wave velocity database for probabilistic assessment of the initiation of seismic soil liquefaction. Proceedings of the 11th International Conference on Soil Dynamics and Earthquake Engineering (The 3rd International Conference on Earthquake Geotechnical Engineering), U. C. Berkeley, CA, U.S.A., Vol. 2: 506-513,.

Lai, C.G., and G. J. Rix (1998) *Simultaneous Inversion of Rayleigh Phase Velocity and Attenuation for Near-Surface Site Characterization*, Report No. GIT-CEE/GEO-98-2, Georgia Institute of Technology, School of Civil and Environmental Engineering, 258 pp.

Pelekis, PC, Athanasopoulos, GA. (2011) An overview of surface wave methods and a reliability study of a simplified inversion technique. Soil. Dyn. Earthquake Eng. (2011), doi:10.1016/j.soildyn.2011.06.012.

Santamarina, J.C., and D. Fratta (1998) Introduction to Discrete Signals and Inverse Problems in Civil Engineering, Amer. Society of Civil Engineers, 327 pp.

Satoh, T.,Poran, C.I.,Yamagata, K.,Rondriquez, JA. (1991) Soil profiling by spectral analysis of surface waves. In: Proceedings Of The Second International Conference On Recent Advances In Geotechnical Earthquake Engineering And Soil Dynamics, Vol.II;1991.p.1429–34.

Viktorov (1967)

Zhdanov, M.S. (2002) *Geophysical Inverse Theory and Regularization Problems*, Methods in Geochemistry and Geophysics, 36, Elsevier, 628 pp.